Journal of Rock Mechanics and Geotechnical Engineering 18 (2026) 3779–3803

Contents lists available at ScienceDirect

Journal of Rock Mechanics and Geotechnical Engineering

journal homepage: www.jrmge.cn

Full Length Article

Online accelerating precursor identification and dynamic probabilistic prediction for rock slope failures using Bayesian inference

Mingxi Chen [a], Zihan Fu [a], Feng Xiong [b], Jie Jiang [a], Qinghui Jiang [c,*]

[a] School of Civil Engineering and Architecture, Guangxi University, Nanning, 530004, China
[b] Faculty of Engineering, China University of Geosciences (Wuhan), Wuhan, 430074, China
[c] School of Civil Engineering, Wuhan University, Wuhan, 430072, China

ARTICLE INFO

Article history:
Received 6 January 2025
Received in revised form
25 June 2025
Accepted 21 August 2025
Available online 24 December 2025

Keywords:
Rock slopes
Accelerating precursor identification
Time-to-failure analysis
Failure probability criterion
Bayesian inference
Inverse velocity (INV) method

ABSTRACT

Timely identification of accelerating precursors and performing reliable time-to-failure analysis are the key components in the management of slope failure risks. This study focuses on rock slope failures and proposes a framework for online identification of accelerating precursors and dynamic probabilistic prediction of failure time grounded in Bayesian inference. By integrating the Bayesian online change-point detection (BOCD) method with a typical dimensionless trend (TDT) model, the BOCD-TDT algorithm is first developed for online identification of acceleration events and their corresponding onset of acceleration (OA). Subsequently, a Bayesian approach is employed to estimate the parameters of the inverse velocity (INV) method, enabling the dynamic probabilistic prediction of slope failure time while quantifying observational and model uncertainties across different accelerating deformation stages. Building on this, the influence of starting point (SP) selection, trend update (TU), and multi-data fusion on prediction reliability is evaluated, and a novel decision criterion for impending slope failure is proposed. The feasibility of the proposed methods is then validated using 73 rock slope failure cases. Results show that using INV data, the BOCD-TDT algorithm can reliably identify acceleration events and the corresponding OA. In time-to-failure analysis, the reliability of dynamic failure predictions can be enhanced by incorporating both observational and model uncertainties corresponding to the deformation stages into the Bayesian prediction model, along with TU detection and multi-data fusion. The proposed failure probability criterion provides valuable guidance for the identification of impending failure and the establishment of ultimate alert thresholds.

1. Introduction

Rock slope failure (e.g. rock slide, rock avalanche, and rock fall) is a globally widespread geological hazard, posing significant threats to human life and property (Zhou et al., 2011; Sättele et al., 2016; Liu et al., 2017; Blondeau et al., 2021). Historical data indicate that out of 38 recorded landslide disasters (from 1000 to 1999) involving over 1000 casualties, 75 % were caused by massive rock slope failure (Evans, 2006). Accurately predicting slope failure time and subsequently formulating early-warning strategies is an effective approach to preventing or mitigating potential losses (Segalini et al., 2018). With the development of monitoring technology, the acquisition of monitoring data on slope movements can provide powerful support for slope failure prediction (Casagli et al., 2023; Lau et al., 2023). However, reliable failure prediction is still highly challenging because the deformation and failure process of rock slopes is controlled by various endogenous/exogenous factors (Donati et al., 2021).

Displacement and its derivatives (i.e. velocity and acceleration) are the most reliable indicators for characterizing slope movement and predicting failure occurrence (Pecoraro et al., 2019). Extensive case observations have shown that displacements occurring in typical rock slopes before imminent failure exhibit a power-law

* Corresponding author.
E-mail address: jqh1972@whu.edu.cn (Q. Jiang).

Peer review under responsibility of Institute of Rock and Soil Mechanics, Chinese Academy of Sciences.

https://doi.org/10.1016/j.jrmge.2025.08.048

divergent phenomenon similar to accelerating creep behavior (Crosta and Agliardi, 2003; Agliardi et al., 2020). Accelerating behavior is considered a precursor of rock slope failure (Carlà et al., 2017a). Therefore, over the past 60 years, scholars and engineers have proposed many empirical or semi-empirical models based on the accelerating creep theory to extrapolate slope failure time, such as Saito's method and its generalizations (Saito, 1965; Fukuzono, 1985; Voight, 1988; Mufundirwa et al., 2010). Despite the emergence of numerous encouraging models for slope failure prediction, their precision cannot be guaranteed, and their real-time predictive performance often proves unsatisfactory (Manconi and Giordan, 2016).

Specifically, there are several reasons that limit the reliability of slope failure prediction using existing models. First, the materials and structures of the rock slopes have spatial variability, resulting in complex geological conditions and topographical features (Jiang et al., 2014; Zhang et al., 2023, 2024a; Chen et al., 2024a, 2024b). With the superposition of seasonal/periodic or episodic triggering factors (e.g. rainfall, groundwater fluctuation, snow melt, excavation, and earthquake), slope deformations exhibit nonlinearity and uncertainty (Gu et al., 2023, 2024; Wang et al., 2023; Hu et al., 2024; Zhou et al., 2024a). Consequently, it is challenging to precisely capture the current/future deformation information and the effect of triggering factors, as well as the mechanical response relationships between them (Ma et al., 2018; Chen et al., 2022). Even during the accelerating deformation stage, which leads to failure, slope deformations exhibit distinct stages or TUs (Rose and Hungr, 2007; Dick et al., 2015). Thus, there is considerable difficulty in the accurate identification of failure precursors. Second, constrained by limitations in data collection, transmission, and processing technologies, survey data and monitoring data from slope sites may be incomplete and inaccurate, potentially affecting the establishment and performance of predictive models (Zheng et al., 2014, 2015; Abdulai and Sharifzadeh, 2019). Additionally, the limitations of model assumptions, errors in parameter estimation, and the lack of user experience can also reduce the reliability of predictive models (Bozzano et al., 2014; Zhang et al., 2020). To sum up, factors such as the complexity of slope deformation and failure process, precursor identification, model assumptions, data limitations, or errors in parameter estimation contribute to the uncertainty of failure prediction.

Accurately identifying the onset of acceleration (OA) during the accelerating deformation stage is one of the key problems in predicting slope failure time (Dick et al., 2015). Presently, several methods have been proposed to identify OA, mainly involving using data filtering or smoothing algorithms to detect change-points or outliers in velocity–time series and then treating them as the OA (Carlà et al., 2017b; Du and Song, 2022; Sharifi et al., 2022). These detection methods provide effective tools for failure prediction; however, the reliable detection of the OA still presents several notable challenges. First, there is limited research on the impact and quantification of uncertainty stemming from errors and noise in raw data on the online detection of OA. Additionally, the long-term evolution of rock slopes often experiences multiple cycles of acceleration and deceleration – from the initial deformation to final failure – under the influence of external triggers (Paronuzzi et al., 2016). This implies that the identified OA may not necessarily correspond to the actual onset of the failure process, potentially leading to erroneous failure time predictions. Therefore, OA identification must incorporate the division and recognition of deformation stages to differentiate between the final acceleration preceding runaway failure and normal acceleration events (Chen and Jiang, 2020; Casagli et al., 2023; Zhang et al., 2024b). Typically, the slope deformation and failure process is categorized into three primary stages – primary, secondary, and tertiary (or accelerating) – based on the characteristics of slope displacement curves that resemble creep behavior (Sullivan, 2007). Furthermore, the accelerating deformation stage can be subdivided into several substages according to the progression of acceleration intensity (Xu et al., 2011; Scoppettuolo et al., 2020). Finally, the ambiguity in failure trends during the initial accelerating deformation stage (Carlà et al., 2017b) raises questions about whether selecting OA as the SP for time-to-failure analysis is the most optimal choice – a matter that requires further discussion.

Quantifying the predictive uncertainties is another critical factor for performing reliable failure prediction (Zhang et al., 2020). Some scholars have recognized the variability in predictive performance among different models and recommend contrasting the predicted values of multiple models to undertake reliable decision-making (Intrieri and Gigli, 2016; Sharifi et al., 2024). Zhang et al. (2022a) organically combined a variety of machine learning methods through the selective ensemble technology of margin distance minimization, significantly improving the prediction effect of slope stability. The effective filtering of data noises is also beneficial in time-to-failure analysis (Du and Song, 2022; Sharifi et al., 2022), but filtering operations are sometimes arbitrary and subjective. Although these methods have somewhat improved failure prediction, most studies still rely on deterministic analysis. Due to the uncertainties arising from endogenous/exogenous factors, the failure time calculated by deterministic models is generally interpreted as only an approximation of actual slope failure timing (Carlà et al., 2018). To address this, several pioneering studies have considered the use of interval or probabilistic prediction instead of traditional deterministic analysis (Carlà et al., 2017b; Zhang et al., 2020; Shen et al., 2023). Carlà et al. (2017b) smoothed monitoring data by means of both short- and long-term moving averages, thereby defining the time interval within which failure could occur. Zhang et al. (2020) employed maximum likelihood estimation to predict the probability distribution of slope failure time by superimposing both observational and model uncertainties. However, the real-time predictive potential of this approach has not yet been systematically evaluated. Shen et al. (2023) employed quantile-based ensemble learning to quantify the uncertainty of the slope safety factor while improving the prediction accuracy. Recently, Bayesian models have also been introduced into slope failure, volcanic eruption, or material failure prediction, yielding preliminary results (Boué et al., 2015; O'Dowd et al., 2021; Zhang et al., 2022b; Zhou et al., 2024b). For instance, Zhou et al. (2024b) utilized Bayesian updating combined with Voight's model to establish a dynamic probabilistic prediction model, quantified the effects of observational uncertainty, and validated the model using three typical landslide cases, but did not account for model uncertainty. Overall, there is currently very limited research on these methods in terms of the impact on the prediction reliability of slope failure, particularly concerning uncertainty analysis across different stages of slope deformations, selection of SPs for calculations, updating of accelerating trends, and fusion of multi-source data. Furthermore, given current technological capabilities, such as monitoring techniques and predictive modeling, a more critical consideration is how to utilize probabilistic prediction information for decision-making or early-warning, rather than concentrating exclusively on achieving highly precise timing predictions.

The rest of the paper is organized as follows. Section 2 provides an overview of the proposed methods and their implementation procedure. Section 3 presents three typical failure cases to exemplify the feasibility of the proposed methods. Section 4 demonstrates the online identification results of accelerating precursors. Section 5 conducts a dynamic probabilistic prediction analysis for slope failure time following the identified OA. Finally, Sections 6 and 7 present the discussion and conclusions of this study.

2. Methodology

2.1. Deformation patterns and deformation stage division of rock slopes

Identifying the deformation pattern and evolutionary stage of a slope is fundamental to conducting time-to-failure analysis. This study focuses on creep rock slopes, excluding the consideration of brittle failure. The trends of the displacement–time (S-t) curve, which comprehensively reflect the entire slope deformation and failure process (i.e. from initial deformation to final failure or restoration of stability), are chosen here to classify the deformation patterns of rock slopes with creep behavior. Creep rock slopes can generally be classified into four representative categories, including three-state creep pattern, progressive deformation pattern, intermittent acceleration–deceleration creep pattern, and regressive convergence pattern, with specific descriptions in Appendix A.

According to the creep theory and existing research, the long-term evolution process of different types of rock slopes is divided into four stages: initial deformation (stage I), steady deformation (stage II), accelerating deformation (stage III), and stable deformation (stage IV) (Saito, 1965; Fell et al., 2000; Intrieri et al., 2019). At stage I, under long-term land surface modifications or sudden triggering by external factors, initial damage occurs in the rock mass, and slope deformation transitions from zero to significant displacement. Rock mass damage develops continuously at stage II, and slope deformation is characterized by slow movements. The displacement–time curve at stage II may undergo minor adjustment or acceleration–deceleration evolution due to occasional or seasonal variations, but the mean deformation velocity remains relatively low. At stage III, the rock slope undergoes rapid or sudden accelerating deformation owing to intermittent damage interpenetrating to form progressive damage, accompanied by severe failure. Additionally, the rock slope can be restored to a state of stability (stage IV) from stages I or II, where the deformation processes either cease or occur at an extremely slow velocity. Slope stabilization can be achieved through natural processes, such as the re-establishment of equilibrium, or through relevant engineering interventions. The stage division of the four types of slope deformation patterns is shown in Appendix A.

Although the above method of stage division aids in understanding the staged characteristics of slope deformation and failure process, it remains within the realm of conceptualization. Recently, an emerging method of interest is the typical dimensionless trend (TDT) model using displacement–time series proposed by Cascini et al. (2014, 2022) to quantitatively divide the stability state of slow-moving landslides, based on common kinematic features of landslides (Fig. 1). To obtain dimensionless displacement D and dimensionless time T, both the displacement segment and the corresponding time interval during the active stages of landslides are normalized as follows:

$$D_{i,j} = \frac{s_{i,j} - s_{0,j}}{s_{p,j} - s_{0,j}} \tag{1}$$

$$T_{i,j} = \frac{t_{i,j} - t_{0,j}}{t_{p,j} - t_{0,j}} \tag{2}$$

where $s_{0,j}$, $s_{p,j}$, $s_{i,j}$, $t_{0,j}$, $t_{p,j}$, and $t_{i,j}$ are the initial, final, and present displacements and the corresponding times of the jth selected stage, respectively. A power-law function with the characteristic exponent m is utilized to fit the dimensionless displacement–time curve:

$$D = T^m \tag{3}$$

The fitting of Eq. (3) requires at least three data points. Three fundamental displacement trends are identified from the magnitude of m, i.e. concave-shaped trend (stable stage) with $0 < m < 1$, linear trend (neutrally stable stage) with $m = 1$, and convex-shaped trend (unstable/accelerating stage) with $m > 1$. Moreover, the convex-shaped trend can be further subdivided into a weakly stable trend for $1 < m < 2$ (substage IIIa), a weakly unstable trend for $2 \leq m < 3$ (substage IIIb), and a strongly unstable trend for $m \geq 3$ (substage IIIc), in terms of the intensity of acceleration. Although originally intended to identify deformation stages of slow-moving landslides, the applicability of TDT to creep-type slope failure has already been demonstrated (Cascini et al., 2022). In this study, the characteristic exponent m is used to dynamically divide the slope deformation stages, which provides support for the identification of accelerating precursors and the quantification of prediction uncertainties.

2.2. Online accelerating precursor identification

To dynamically identify accelerating precursors in the slope deformation, this study proposes an online identification algorithm integrating a Bayesian changepoint detection (BOCD) method with the TDT model, termed the BOCD-TDT algorithm. BOCD is first utilized to identify one or more changepoints in a time series as candidates for OA. Subsequently, TDT is initiated to determine whether the changepoint is an OA and to identify the current deformation stage of the slope. The characteristic exponent $m > 1$ indicates the emergence of accelerating deformation.

The Bayesian approach for changepoint detection is appealing due to its ability to characterize the uncertainty in the evolution of time series (Fearnhead, 2006). In this study, the widely used BOCD method proposed by Adams and MacKay (2007) is selected for changepoint detection. BOCD incorporates new observations in real time and then updates the prior distribution of historical data to determine whether the new data originate from a new or previous distribution. As each new observation is added to the detector in the time series $\boldsymbol{x}$, a distribution of run length r_t for the current regime is created. Within the given time step t, if the time series continues its original trend, r_t increases by 1 (growth); if a changepoint occurs, r_t drops to 0 (changepoint), as shown in Fig. 2. Since retrospective segmentation of the time series is not required, BOCD allows for the precise online inference of the most recent changepoint. The observed points corresponding to the end of the continuous increase in r_t are regarded as the potential OAs (red dots in Fig. 2b). The specific modeling and parameter calibration details of BOCD are presented in Appendix B.

TDT calculation is performed simultaneously with the detection of changepoints to identify acceleration events and subsequently determine the OA. The detailed calculation steps are as follows:

(1) Starting from the initial observation, new observations are continuously incorporated, and the TDT is calculated in real time until a changepoint occurs.
(2) Once a changepoint is detected, the SP for performing TDT is updated to the changepoint until the next changepoint appears.
(3) When an acceleration event is detected, the calculated results of TDT are assessed and interpreted, especially in cases where multiple acceleration events occur within the deformation pattern. This includes determining the current deformation stage of the slope and assessing whether this

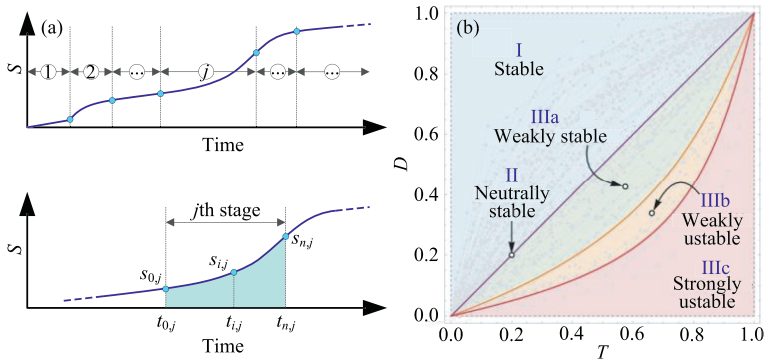

Fig. 1. Kinematic characterization of landslides using dimensionless displacement curves (Cascini et al., 2022).

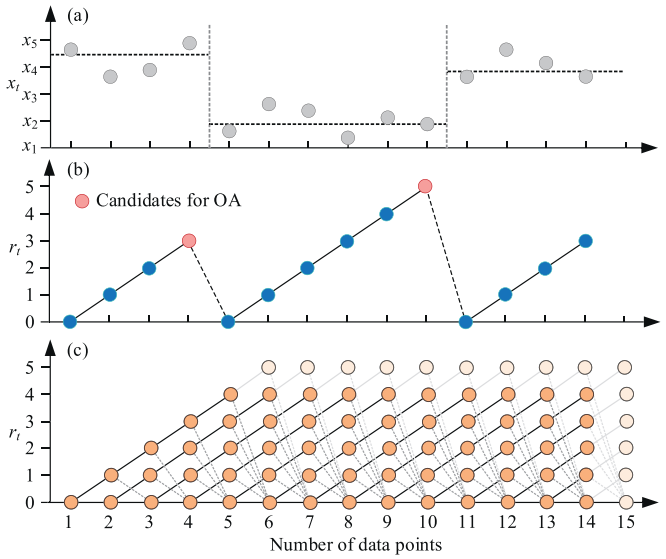

Fig. 2. Schematic diagram for implementing BOCD (Adams and MacKay, 2007).

acceleration is trending toward failure. Additionally, to enhance the robustness of identification of acceleration events (such as disturbance from data noise and fitting errors in TDT), it is assumed that acceleration events can only be identified when m is persistently greater than 1.05 with the corresponding changepoint confirmed as OA.

(4) Research indicates that the slope deformation trend in some cases is also updated during the accelerating deformation stage (Dick et al., 2015). To address this issue, the multi-track TDT calculation is conducted. First, after a new changepoint is identified, the TDT following OA (TDT_{OA}) continues to update without interruption. Synchronously, a new TDT (TDT_N) is added after the new changepoint is detected. Then, m values calculated from TDT_{OA} and TDT_N are compared. If both TDT_{OA} and TDT_N show a continuous increase in m and $m > 1$, it is considered that the sustained acceleration trend has not stopped. Conversely, if the m from TDT_{OA} decreases, and the m from TDT_N also shows a decreasing trend or $m < 1$, it is concluded that the acceleration trend has ceased. At this time, updates to TDT_{OA} can be halted. This method can enhance the reliability of accelerating the precursor while also enabling automatic online judgment.

2.3. Bayesian estimation of slope failure time

In this study, the inverse velocity (INV) method proposed by Fukuzono (1985) is selected to predict the failure time of rock slopes during the accelerating deformation stage. This method has been extensively applied in engineering practice because of its concise mathematical form and ease of use. Its mathematical expression is as follows:

$$\Lambda = \left[A(\alpha-1)\left(t_f - t\right)\right]^{\frac{1}{\alpha-1}} \tag{4}$$

where Λ is the inverse of deformation velocity v, i.e. $\Lambda = 1/v$; t_f is the predicted failure time; and A and α are the constant parameters related to material properties, scale, and deformation patterns of rock slopes. The linear INV (LINV) method with $\alpha = 2$ is commonly used in practical applications due to its simplicity, as well as the inability of the nonlinear trend to achieve higher and more robust predictive accuracy (Rose and Hungr, 2007; Chen and Jiang, 2020). Let $\alpha = 2$, then Eq. (4) reduces to

$$\Lambda = A\left(t_f - t\right) \tag{5}$$

As mentioned earlier, there is an error ε between the predicted failure time t_f obtained by LINV and the actual failure time T_f because of various influencing factors. Drawing from the research of Zhang et al. (2020), sources of ε are categorized into observational uncertainty ε_o (stemming from observation errors and environmental noises) and model uncertainty ε_m (stemming from model assumptions), where both ε_o and ε_m are normally distributed random variables.

To consider the contribution of ε_o to the prediction, Eq. (5) is rewritten as

$$\Lambda = A\left(t_f - t\right) + \varepsilon_o \tag{6}$$

where ε_o is the normally distributed random variable, following $N(0, \sigma_0^2)$.

Based on Bayes' theorem, using the prior information of $\boldsymbol{\theta}$ (i.e. A, α, and σ_0) and the observational data $\boldsymbol{D} = \{d_1, d_2, \ldots, d_j\}$, where j is the number of observational data, the posterior distribution $p(\boldsymbol{\theta}|\boldsymbol{D})$ of the LINV parameters is

$$p(\boldsymbol{\theta}|\boldsymbol{D}) = \lambda p(\mathbf{D}|\boldsymbol{\theta}) p(\boldsymbol{\theta}) \tag{7}$$

where λ is the normalized parameter, $p(\boldsymbol{\theta})$ is the prior distribution, and $p(\boldsymbol{D}|\boldsymbol{\theta})$ is the likelihood function. $p(\boldsymbol{D}|\boldsymbol{\theta})$ is given by

$$p(\boldsymbol{D}|\boldsymbol{\theta}) = \prod_{j=1} \phi\left(\frac{d_j - A\left(t_f - t_j\right)}{\sigma_0}\right) \tag{8}$$

It is assumed that the prior distributions for both A and t_f are improper uniform distributions with a lower bound of 0, and the prior distribution for σ_0 follows a normal distribution with a mean of 0 and a standard deviation of 1. The posterior parameter estimation of Eq. (8) is performed using the Metropolis-Hastings algorithm, which is a popular Markov Chain Monte Carlo (MCMC) method for obtaining a sequence of random samples from a probability distribution (Metropolis et al., 1953; Hastings, 1970). The length of the Markov chain is 50,000, and the first 10,000 samples are discarded to eliminate the influence of the initial points.

To facilitate the calibration of model uncertainty, it is assumed that the random samples of the posterior distribution of t_f follow a normal distribution. A total of n failure cases are used to quantify model uncertainty. According to the study by Zhang et al. (2020), model uncertainty ε_m is also assumed to follow a normal distribution $N(\mu_m, \sigma_m^2)$. Let $\boldsymbol{\Omega} = \{\mu_m, \sigma_m\}$. For the ith case ($i = 1, 2, \ldots, n$), assuming that the actual failure time T_{fi} follows a normal distribution $N(\mu_{ai}, \sigma_{ai})$, and the predicted failure time t_f also follows a normal distribution $N(\mu_{fi}, \sigma_{fi}^2)$, the relationship between T_f and t_f is as follows:

$$\left.\begin{aligned} \mu_a &= \mu_f + \mu_a \\ \sigma_a &= \sqrt{\sigma_f^2 + \sigma_m^2} \end{aligned}\right\} \tag{9}$$

The model uncertainty $\boldsymbol{\Omega}$ can be calculated as follows:

$$p\left(T_{fi}|\boldsymbol{\Omega}\right) = \phi\left(\frac{T_{fi} - \mu_{ai}}{\sigma_{ai}}\right) \tag{10}$$

To calibrate both observational and model uncertainties across different accelerating deformation substages, a foundational database is developed by collecting 70 rock slope failure cases from the scientific literature, as detailed in Appendix C. Subsequently, the proposed probabilistic failure time prediction method dynamically calculates failure time and the corresponding observational uncertainty for continuously updated observational data according to the OA. Based on this, model uncertainty for different deformation substages is then calibrated using Eq. (10).

The framework for online accelerating precursor identification and dynamic failure time prediction of rock slopes is illustrated in Fig. 3.

3. Three rock slope failure cases outside the database

In addition to the database, three rock slope failure cases are considered to further test the reliability of the proposed probabilistic failure time prediction method and to demonstrate the implementation process of online accelerating precursor identification. The deformation patterns of these three failure cases include the three-state creep pattern (Jimingsi landslide), progressive deformation pattern (Zhouzhi landslide), and intermittent acceleration–deceleration creep pattern (Vajont landslide).

3.1. Case 1: Jimingsi landslide

Jimingsi landslide is a typical translational landslide, situated on the south bank of the Yangtze River in Zigui County, Hubei Province, China (Fig. 4) (Qin et al., 2006). The lithology is composed of thick-bedded limestone interbedded with soft marlite. The elevations of the leading and trailing edges of the landslide are 250 m and 480 m, respectively. Slope angles of the original slope range between 35° and 55°, coinciding with the dip angle of the rock formation. In this study area, the rock mass structures are fragmented with well-developed faults and fractures. In particular, fault F4 plays a controlling role in forming the landslide boundary. Due to long-term limestone mining activities, the sliding mass experienced a creep sliding-tension deformation. In early May 1991, the sliding mass exhibited a sharply accelerating deformation behavior under the influence of heavy rainfall and finally detached from the mountain at about 4:58 a.m. local time on June 29, 1991. The typical cumulative displacement–time, velocity–time, and inverse velocity–time curves recorded from early April 1990 to imminent failure are shown in Fig. 5 (Xu et al., 2011). The displacement–time curve of the Jimingsi landslide displays a typical three-state creep pattern.

3.2. Case 2: Zhouzhi landslide

The Zhouzhi landslide is located along the G108 National Highway in Zhouzhi County, Shaanxi Province, China (Yu et al., 2019). It has a position elevation of about 750 m, with a relative elevation difference of about 127 m from the water surface of the Heihe reservoir (Fig. 6). The sliding mass is composed of Lower Proterozoic sericite quartz schist covered with Quaternary residual slope deposits. Sericite quartz schist is a type of soft rock that is prone to softening and weathering. The attitude of the rock formation is 225°–230°∠45°–50°. The slope surface of this landslide has a dip angle of 145°–150°, and its inclination is nearly perpendicular to that of the rock formation. The study area is tectonically active. The Youfanggou–Huangtai fault zone passes through the southern part of this landslide, with an attitude of NW∠50°–60°. Several cracks have developed on the ground surface. A local collapse has already occurred in this area due to rainfall in October 2017, indicating that the original slope is already in an unstable state. To prevent landslides from threatening passing vehicles, potentially unstable areas have been monitored using the global navigation satellite system (GNSS) since December 15, 2017. Four monitoring stations are installed on the ground surface. At 4:00 a.m. local time on February 19, 2018, a new local collapse occurred on the right side of the landslide. The cumulative displacement–time, velocity–time, and inverse velocity–time curves obtained from monitoring stations in the collapse area are shown in Fig. 7. It can be observed that the displacement–time curves exhibit a typical progressive deformation pattern.

3.3. Case 3: vajont landslide

The Vajont landslide is one of the most famous landslides in history due to its complex failure mechanisms and catastrophic impacts, including significant economic losses and human casualties (Massironi et al., 2013; Paronuzzi et al., 2016; Carlà et al., 2017b; Bak et al., 2019). This landslide is located on the left bank of the Vajont Valley (Eastern Italian Alps), Friuli Venezia Giulia, Italy (Fig. 8). A vast limestone rock mass with a volume of approximately 2.7×10^8 m^3 detached from the slope of Mount Toc at about 10:39 p.m. local time on October 9, 1963, and slid into the Vajont reservoir at a speed of around 110 km/h. The enormous sliding mass filled the reservoir in a very short time, causing the dam to overflow and triggering a tsunami wave of 5×10^8 m^3, which destroyed seven villages in the Piave Valley and resulted in approximately 2500 deaths. Records of cumulative displacement (and velocity/inverse velocity)–time curves and reservoir water level are well-documented in the literature for the period between the initial impoundment to the runaway failure in the Vajont landslide, as shown in Fig. 9. Notably, the movement of the sliding

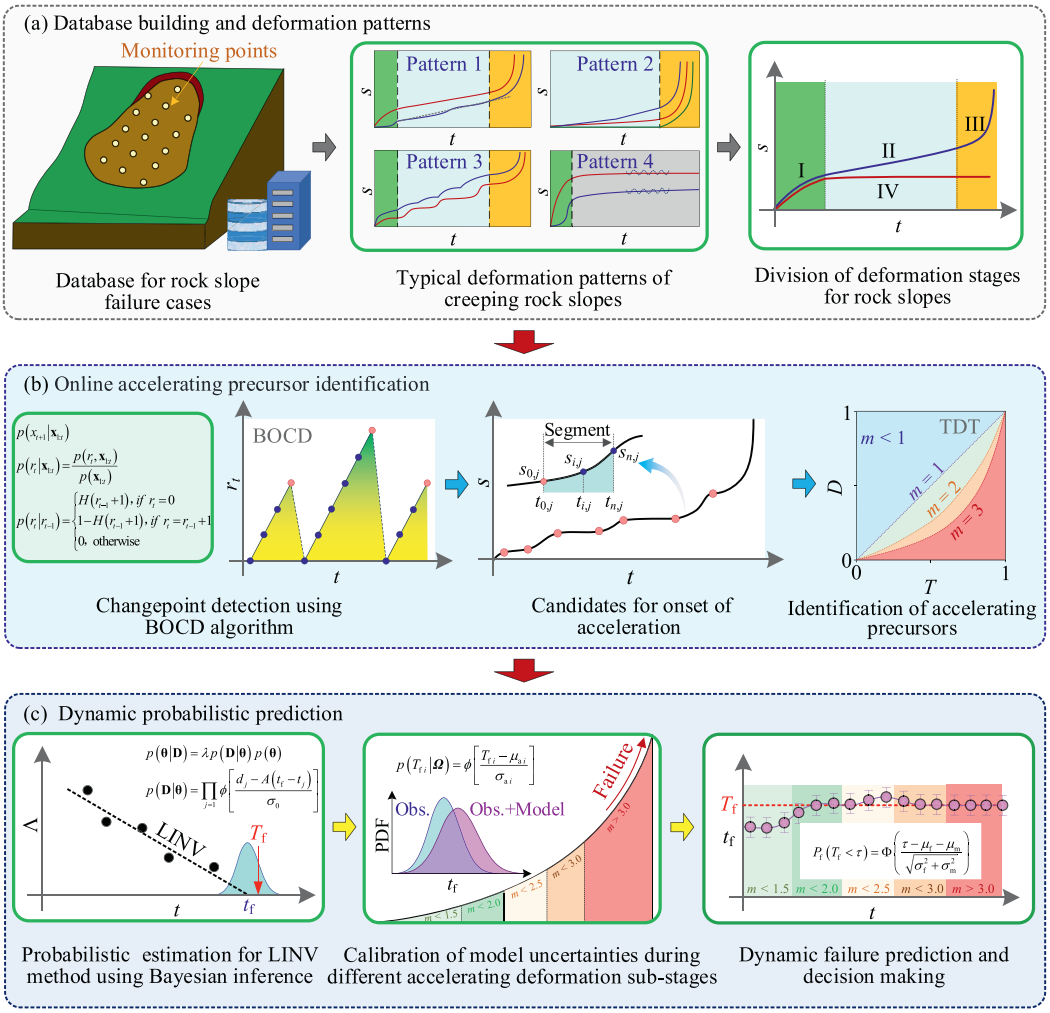

Fig. 3. Flowchart for the identification of OA and dynamic probabilistic prediction.

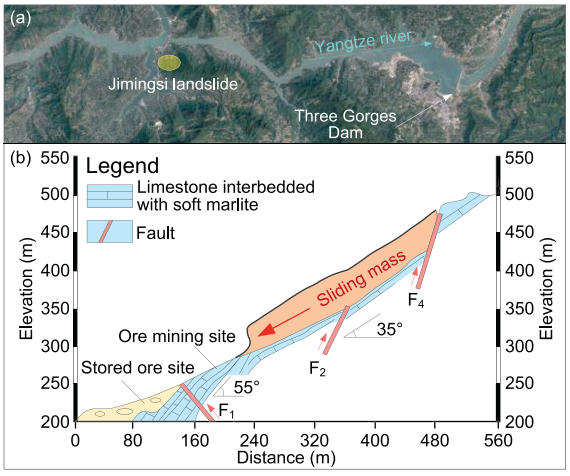

Fig. 4. Overview of Jimingsi landslide: (a) Location of Jimingsi landslide; and (c) Geological cross-section (modified from Qin et al., 2006).

mass was strongly controlled by the reservoir water impoundment with a positive correlation between its deformation and the rise in the reservoir water level. The Vajont landslide exhibits a typical intermittent acceleration–deceleration creep pattern, with the displacement–time curve exhibiting continuous slow development (during the dead water level period) and intermittent stages of deceleration (during the drawdown period) and acceleration (during the filling period).

4. Results of online accelerating precursor identification

The above three failure cases (Jimingsi landslide, Zhouzhi landslide, and Vajont landslide) are used to illustrate the implementation of the BOCD-TDT algorithm and validate its performance in detecting accelerating precursors. Three types of time series, namely, displacement–time, velocity–time, and inverse velocity–time series, are utilized to test the sensitivity of the BOCD-TDT algorithm.

4.1. Precursor identification in the Jimingsi landslide

The precursor identification results using the displacement–time, velocity–time, and inverse velocity–time series, respectively, are shown in Fig. 10. It should be noted that the run length (maximum probability curve), r_t, in Fig. 10 does not develop linearly because the time intervals between the monitoring data points are not evenly spaced. The BOCD algorithm assumes that the time intervals between data points are evenly spaced. Thus, in an ideal scenario, the r_t would appear as a sloped straight line.

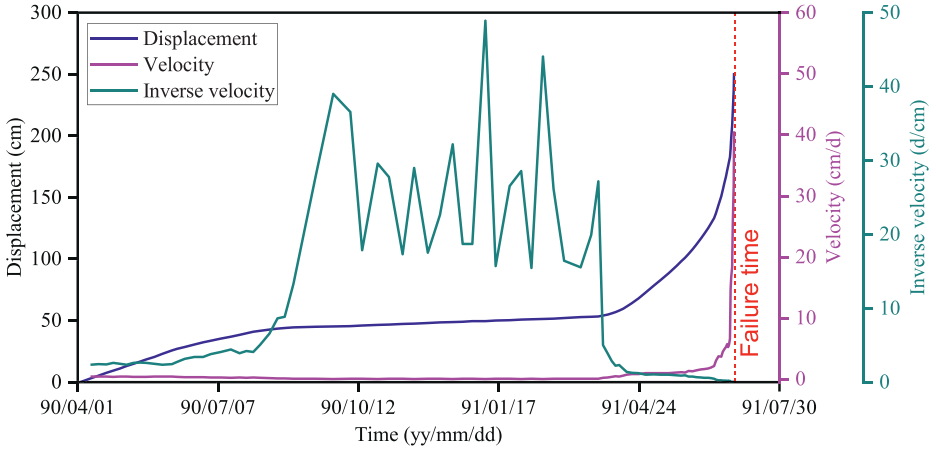

Fig. 5. Cumulative displacement–time, velocity–time, and inverse velocity–time curves before failure in Jimingsi landslide.

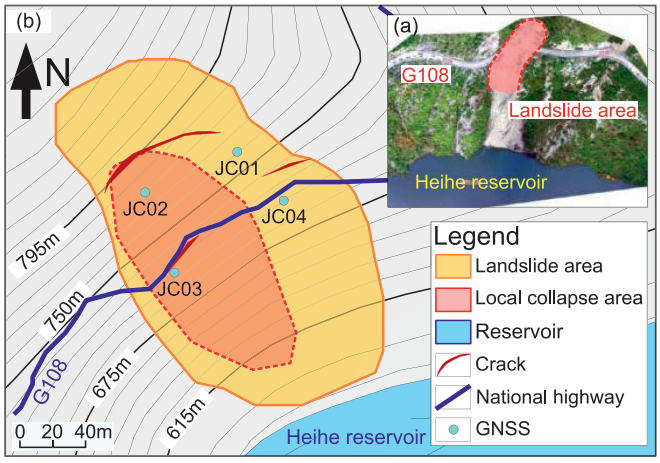

Fig. 6. Overview of the Zhouzhi landslide (modified from Yu et al., 2019): (a) Location of the Zhouzhi landslide; and (c) Geological map.

The OA candidate points (CPs) identified from the three types of time series, namely CP_S, CP_v, and CP_A, during the accelerating deformation stage are shown in Fig. 11.

From the displacement–time series (Fig. 10b), two changepoints are detected, but their positions differ considerably from the transition points between the different deformation stages (stages I, II, and III). In particular, the timing of the detected CP_S has a significant delay compared to the occurrence of OA (Fig. 11). From the velocity–time series, no changepoint is detected between stages I and II as the transition velocity between the two stages is relatively small. All three changepoints are detected from the accelerating deformation stage. The first changepoint is located close to the OA, while the other two changepoints correspond to the positions where trends in the velocity–time series are updated. More changepoints are detected in the inverse velocity–time series. Using the inverse velocity–time series allows for more reliable identification of the transition points between the three deformation stages with shorter delays. The identified location of CP_A is very close to the occurrence of the true OA. In short, for the three-state creep pattern, the signals of the initial accelerating deformation stage can be detected from all three types of time series, but OA identification using inverse velocity data has higher sensitivity.

The results after dynamic updating of the characteristic exponent m are shown in Fig. 10e. In this case, changepoints used for updating TDT calculation are obtained from inverse velocity–time series. TDTs for the 1st and 2nd updates corresponding to stages I and II have m values that are less than 1, except for two data points at the end of the 2nd update, where m exceeds 1, due to a certain delay in the online identification of OA. The updates of the last three TDTs occur during the accelerating deformation stage. In the

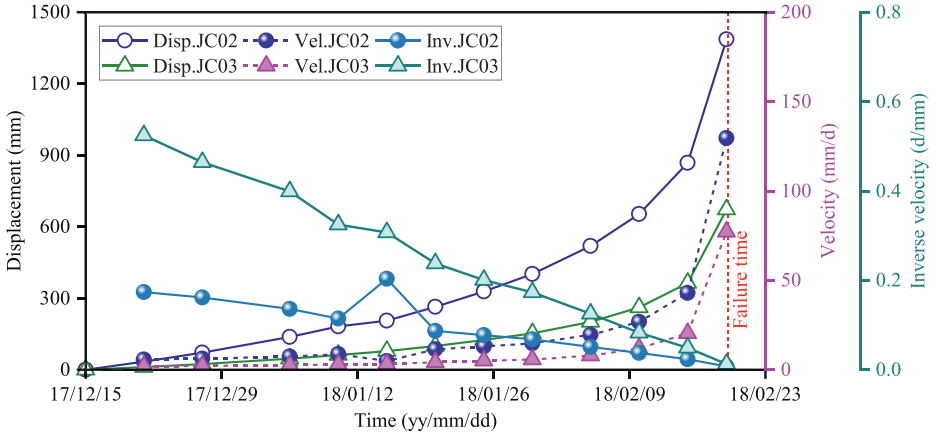

Fig. 7. Cumulative displacement–time, velocity–time, and inverse velocity–time curves before failure in the Zhouzhi landslide.

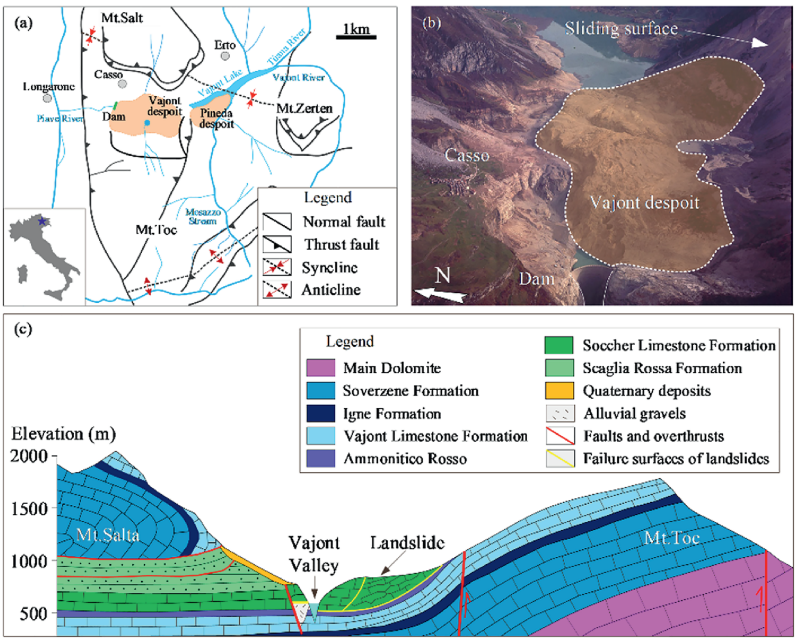

Fig. 8. Overview of the Vajont landslide: (a) Location of the Vajont landslide (modified from Massironi et al., 2013); (b) Schematic diagram of the landslide area (modified from https://www.ilpost.it/2013/10/09/il-disastro-del-vajont/vajont-dam/); and (c) Geological section of the Vajont landslide prior to failure (modified from Bak et al., 2019).

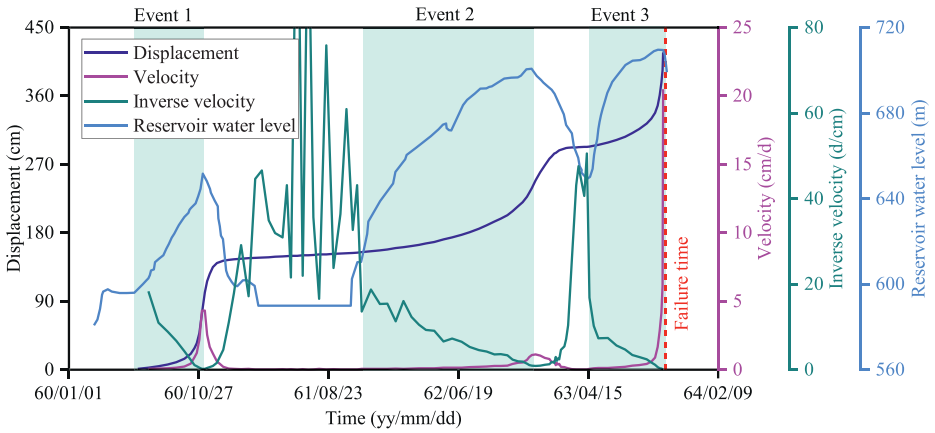

Fig. 9. Cumulative displacement (velocity/inverse velocity)–time curves, and reservoir water level in Vajont landslide.

3rd update, m remains consistently greater than 1.05, and its value exceeds 5 at the last observation. In the 4th and 5th updates, m values continue to increase and remain above 1, implying that these two are only updates of the accelerating trend rather than the cessations of acceleration.

4.2. Precursor identification in the Zhouzhi landslide

The precursor identification results using the displacement–time, velocity–time, and inverse velocity–time series in the Zhouzhi landslide, respectively, are shown in Fig. 12. From the inverse velocity–time series (Fig. 12a), it is evident that this landslide continued to accelerate until its final failure. Theoretically, the first observation point is the OA, and there are no other changepoints that serve as candidates for OA. No changepoint is detected in either the displacement–time or velocity–time series, which is as expected. However, a changepoint is detected in the velocity–time series, representing an unprecedented acceleration that occurs before the impending failure. On the whole, BOCD effectively captures the evolution law of the progressive deformation pattern.

The results of dynamic updating of the characteristic exponent m obtained from inverse velocity–time series are shown in Fig. 12e m consistently remains above 1.05 throughout the observation period, and is greater than 3 in the last observation, clearly indicating the imminent failure of Zhouzhi landslide. In the early stage, m is relatively low ($m = 1.05–1.2$), corresponding to a gradual increase in deformation velocity, with an average daily rise of 1 mm/d. Visually, the earlier monitoring data of displacement–time and velocity–time series show a pattern of steady deformation (Fig. 12a). However, upon closer examination, this actually represents a phase of slowly accelerating deformation, which explains the relatively low m values. Instead, the inverse velocity–time series clearly displays the initial acceleration trend. Thus, this result highlights the critical importance of incorporating inverse velocity data into slope risk management, especially during the initial accelerating deformation

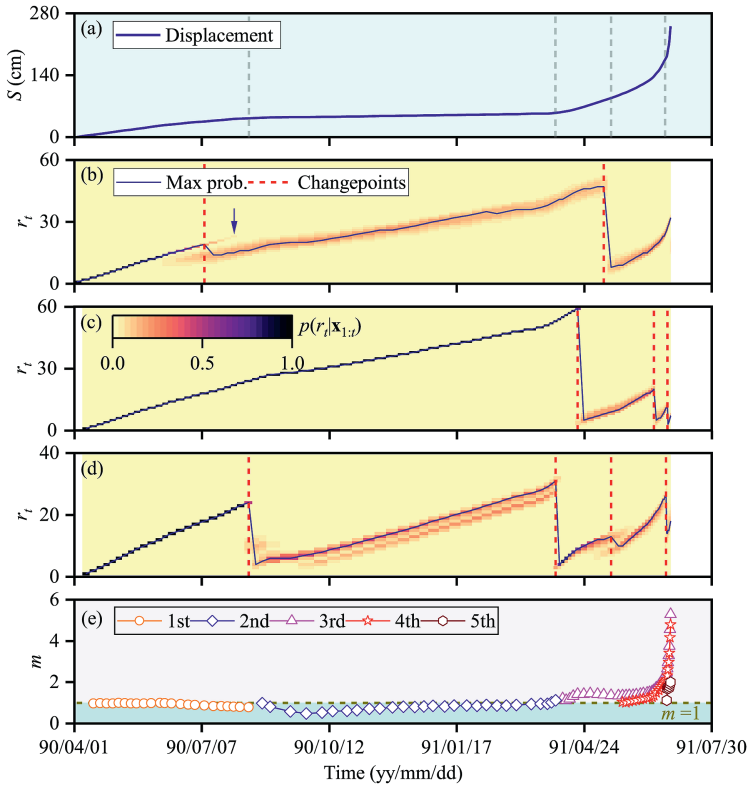

Fig. 10. Online accelerating precursor identification in Jimingsi landslide: (a) Displacement–time, velocity–time, and inverse velocity–time series; (b–d) The heatmaps of changepoint detection results from the displacement–time, velocity–time, and inverse velocity–time series, respectively; and (e) The m values that are dynamically updated based on changepoint detection results from the inverse velocity–time series. The gray dashed lines represent the positions of changepoints identified from the inverse velocity–time series. The heatmaps show the posterior probability of the current run $p(r_t|\boldsymbol{x}_{1:t})$ at each time step. The navy-blue solid lines in the heatmaps represent the maximum probability of r_t continuing to increase, and the red dashed lines indicate the most likely positions where the changepoints occur.

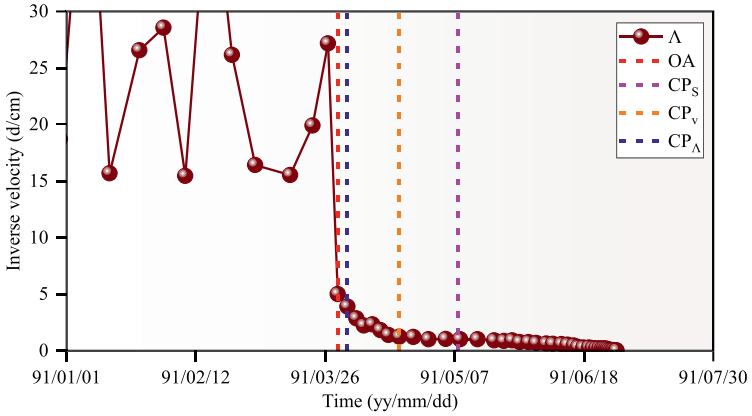

Fig. 11. Relative positions of OA and three detected changepoints.

stage when the failure trend is not apparent.

4.3. Precursor identification in the vajont landslide

The online changepoint detection results using the displacement–time, velocity–time, and inverse velocity–time series in the Vajont landslide, respectively, are shown in Fig. 13.

Two changepoints are detected from the displacement time series, which are located in the first two accelerating deformation periods. BOCD can only approximately capture the time points at which shifts in the long-term deformation evolution trends of rock slopes occur from the displacement–time series. However, these two changepoints reasonably divide the deformation trend of the Vajont landslide into three stages.

From the velocity–time series, five changepoints are detected. BOCD can detect the evolutionary law of acceleration–deceleration deformation during the 1st and 3rd reservoir impoundment periods. The detection timing of the 4th changepoint is very close to the OA of the accelerating deformation stage prior to failure. For the 2nd reservoir impoundment period, although BOCD detects the acceleration event, it fails to capture the deformation characteristic transitioning from acceleration to deceleration during the

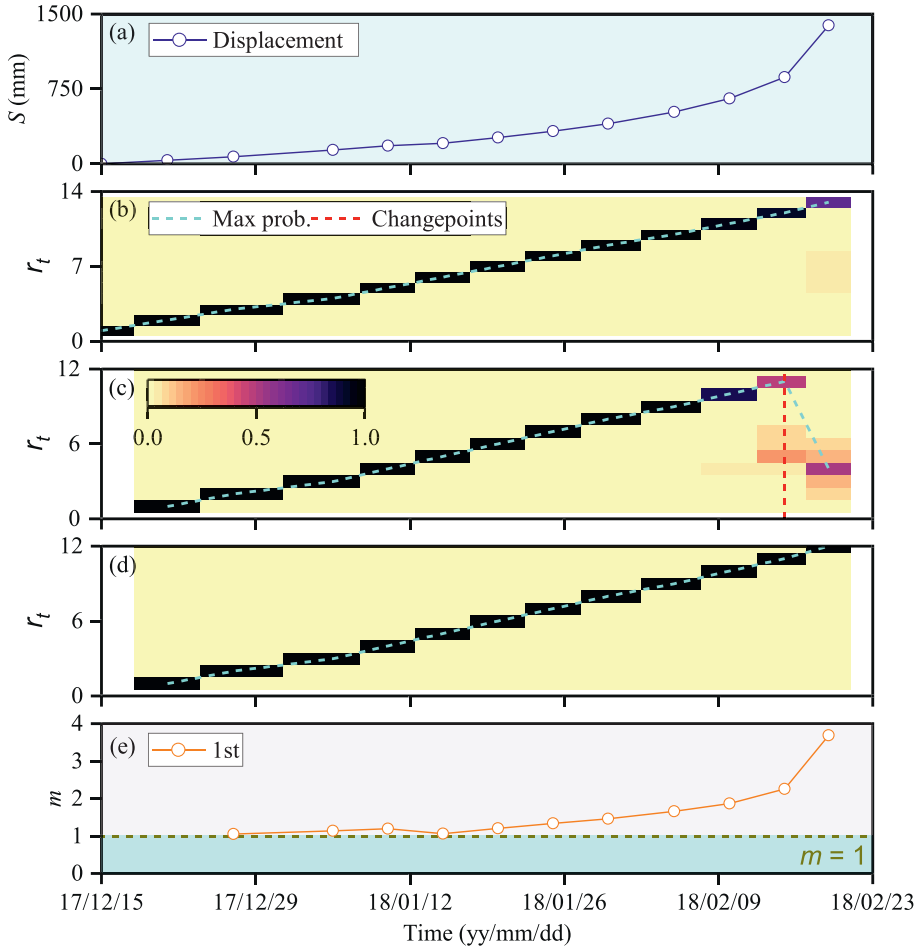

Fig. 12. Online accelerating precursor identification in Zhouzhi landslide.

drawdown operation. This is because, compared to the other two acceleration events, the 2nd acceleration event involves a slow acceleration process, resulting in relatively smaller velocity values. This result further validates that BOCD has a higher sensitivity to time series with sharp changes evident.

Consistent with the previous two cases, BOCD can obtain more accurate changepoint information from the inverse velocity–time series and detects 10 changepoints. From the relative positions of the changepoints (gray dashed lines in Fig. 13a) and the displacement and inverse velocity–time series, it can be observed that the detected changepoints effectively capture the key points of the deformation trend change. Overall, except for the two changepoints indicating TUs during the 2nd and 3rd acceleration events, the other changepoints reasonably segment the kinetic characteristics of the Vajont landslide.

The results of dynamic updating of the characteristic exponent m obtained from inverse velocity–time series are shown in Fig. 13e. TDTs undergo two updates during the first accelerating deformation stage. The m of the 1st update increases continuously from 1.42 to 7.71, while the m of the 2nd update gradually decreases over time. According to the study by Cascini et al. (2022), $m \geq 3$ shows a strongly unstable trend in slope deformation. Additionally, the pre-existing sliding surface before reservoir impoundment and the strong sensitivity of deformation to the fluctuations in the reservoir water level suggest that the Vajont landslide was already in an extremely dangerous state during the initial impoundment period. For the 2nd accelerating deformation period, changepoint detection is relatively complex, with a total of four changepoints detected. Nevertheless, the multi-track TDT calculations reliably identify the duration of the acceleration events. m increases from an initial value of 1.2–2.92, indicating a weakly unstable trend in slope deformation. During the 3rd accelerating deformation period, TDTs undergo three updates. In the 8th update, the m reaches 10.39 in the last observation. Regarding failure time prediction, the 9th update of the TDT obtains ideal results because the inverse velocity data after the 9th changepoint (OA) are arranged in an approximately straight line.

According to the analysis of the three historical cases above, it can be concluded that the proposed BOCD-TDT algorithm effectively divides the kinetic behaviors of three types of creep rock slopes (three-state creep pattern, progressive deformation pattern, and intermittent acceleration–deceleration creep pattern) during different deformation stages, and in turn, reliably identifies acceleration events and their corresponding OA. For online detection of changepoints, the sensitivity of the BOCD to displacement–time, velocity–time, and inverse velocity–time series increases in this order. Therefore, inverse velocity data are recommended for the online identification of acceleration events. Moreover, when using displacement data for detection, the proposed method can provide a more reasonable division of the sub-deformation stages in the long-term evolution of creep rock slopes.

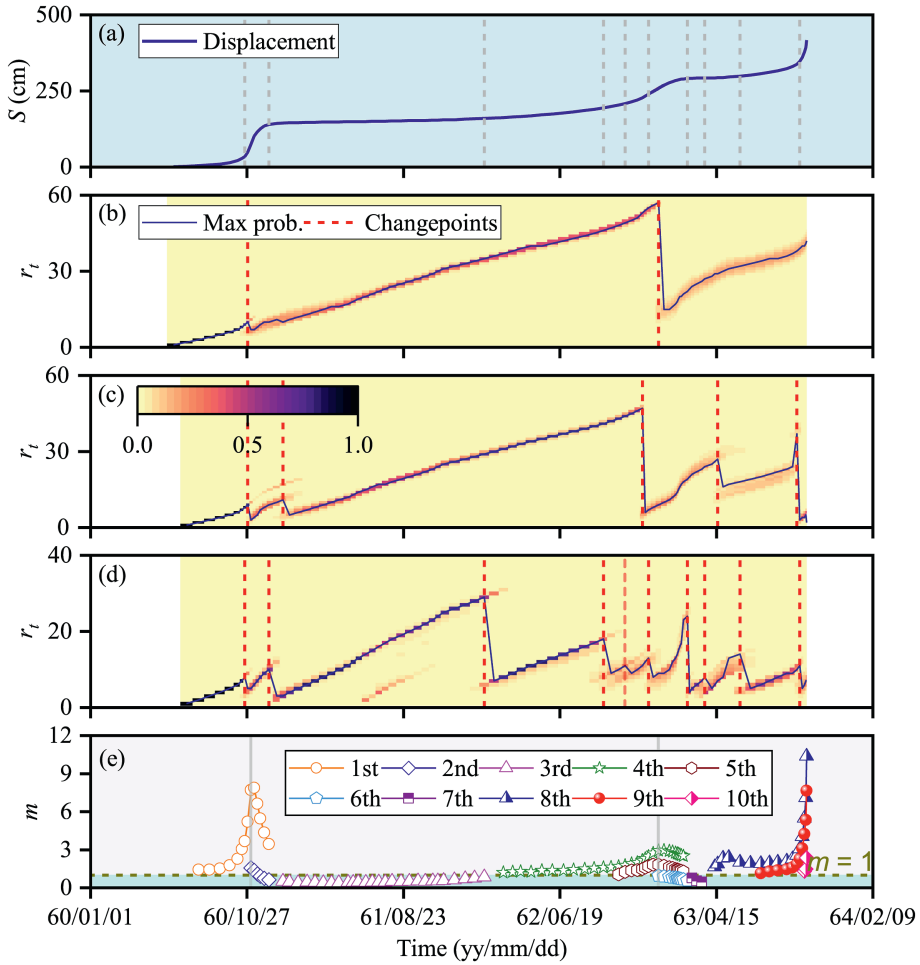

Fig. 13. Online accelerating precursor identification in the Vajont landslide.

5. Dynamic probabilistic failure time prediction

5.1. Uncertainty characterization of predicted failure time

To calibrate the model uncertainty of the LINV method during different accelerating deformation substages, 70 failure cases from the established database are used to calibrate the observational uncertainties of t_f. The observational data during the accelerating deformation stage are divided into five observed time intervals, namely $T_{1.5} = [t_{OA}, t_{m=1.5}]$, $T_2 = [t_{OA}, t_{m=2}]$, $T_{2.5} = [t_{OA}, t_{m=2.5}]$, $T_3 = [t_{OA}, t_{m=3}]$, and $T_{last} = [t_{OA}, t_{last}]$, where t_{OA} represents the observed time at OA, $t_{m=1.5}$, $t_{m=2}$, $t_{m=2.5}$, $t_{m=3}$, and t_{last} are the observed times when m reaches 1.5, 2, 2.5, 3, and the last observation, respectively. It should be noted that in certain cases, one or two observation intervals may be missing due to sparse and scattered monitoring data, cessation of monitoring before m reaches 3, or even slope failure occurring when $m < 3$. However, each observed time interval used for statistical analysis contains at least 50 historical cases, ensuring statistical significance. The relationship between the predicted failure time t_f and the actual failure time T_f in each observed time interval is shown in Fig. 14. In the overall trend, as m increases, the slope k of the fitting line $t_f = kT_f$ gradually approaches 1, and the coefficient of determination R^2 also increases. This implies that the closer the observed time to T_f, the higher the predictive accuracy. When the time interval T_2 and beyond is used, the LINV method can obtain relatively reliable predictive results.

Subsequently, t_f and T_f obtained from different observed time intervals for each case are substituted into Eq. (21) to calculate the model uncertainty. The normal distributions of the model uncertainties obtained from different observed time intervals are illustrated in Fig. 15. The model uncertainties calculated for the observed time intervals $T_{1.5}$, T_2, $T_{2.5}$, T_3, and T_{last} are as follows: $N(7.27\text{ d}, 9.68^2\text{ d}^2)$, $N(3.42\text{ d}, 3.63^2\text{ d}^2)$, $N(2.12\text{ d}, 2.61^2\text{ d}^2)$, $N(2.11\text{ d}, 2.7^2\text{ d}^2)$, and $N(1.02\text{ d}, 1.43^2\text{ d}^2)$, respectively. Consistent with the fitting results in Fig. 14, the model uncertainty generally decreases as m increases.

When $m > 2$, the kinetic behavior of slope deformation is classified as a weakly stable trend, and the corresponding mean value of model uncertainty is only 3.42 d, at which point the LINV method can provide reliable failure probabilistic prediction. The mean value and standard deviation of the model uncertainty for T_{last} are both relatively small, indicating that once the slope deformation is in a strongly unstable trend ($m > 3$), a deterministic failure prediction can be conducted. Additionally, the mean value of model uncertainties for each observed time interval is greater than 0, indicating that the LINV method is a conservative predictive model. From the above analysis, it can be concluded that even when using the last observation before impending failure to perform time-to-failure analysis, the model uncertainty cannot be ignored.

This study proposes that both observation and model uncertainties should be considered simultaneously in dynamic prediction, with the model uncertainty being updated as the deformation stage develops. The results of the probability density

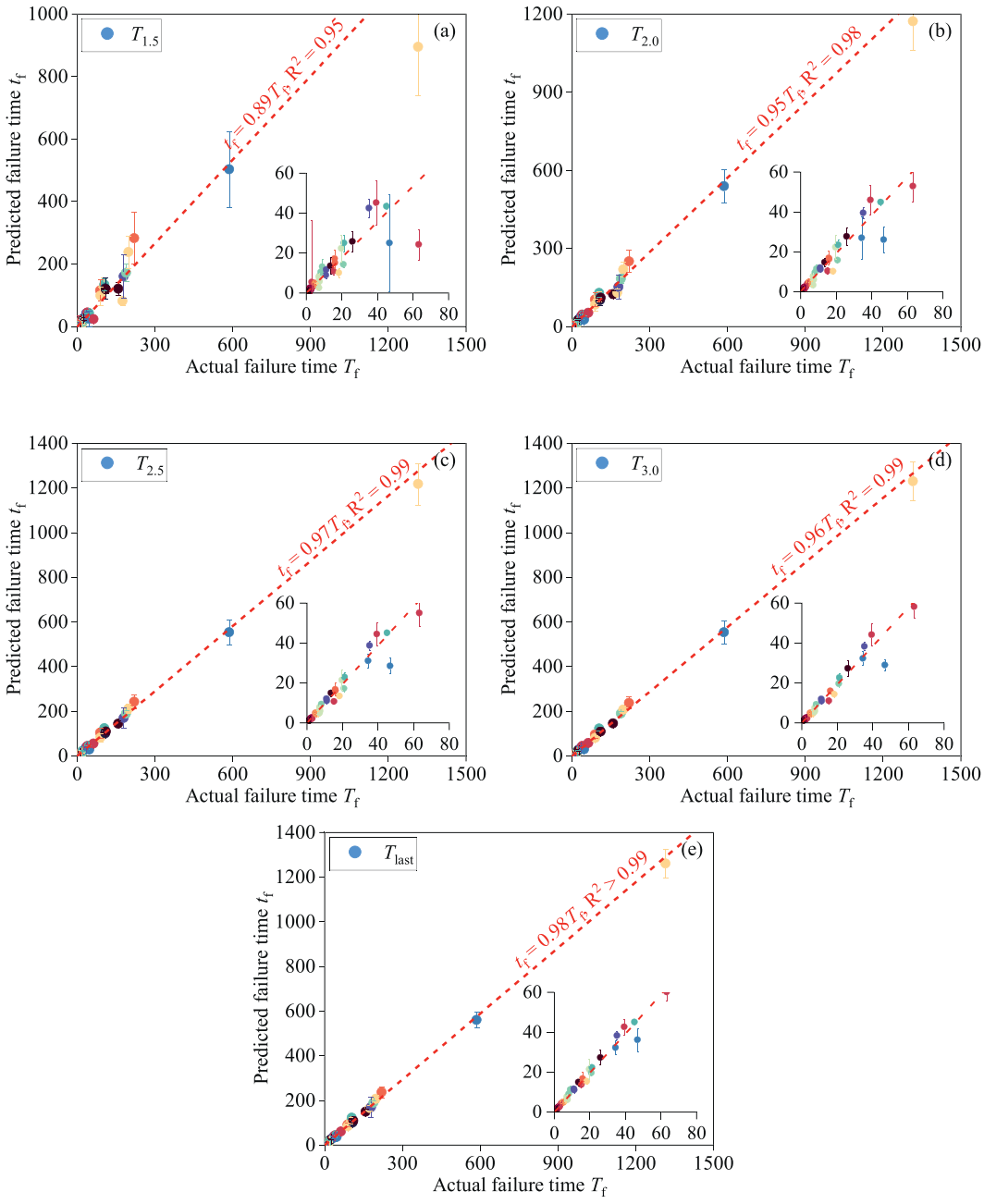

Fig. 14. Relationship between t_f and T_f in each observed time interval.

function (PDF) and cumulative distribution function (CDF) of t_f, calculated with and without considering model uncertainty, are shown in Fig. 16. As can be observed, considering model uncertainty enhances the ability of the prediction interval to contain t_f. To further validate the feasibility of the proposed method, predictive results for different observed time intervals are calculated using all failure cases in the database. The predictive results are quantified using normalized failure time t_{norm} to facilitate comparison (Zhang et al., 2022b):

$$t_{norm} = \frac{2T_f - \left(t_{fU} + t_{fL}\right)}{t_{fU} - t_{fL}} \tag{11}$$

where t_{fU} and t_{fL} represent the upper and lower bounds of the 95 % confidence interval (CI) for the predicted failure time, respectively; t_{norm} in [−1, 1] indicates that the 95 % CI of t_f contains T_f; t_{norm} in $(-\infty, -1)$ indicates that T_f is earlier than the lower bound of the 95 % CI for t_f; and t_{norm} in $(1, +\infty)$ indicates that T_f is later than the upper bound of the 95 % CI for t_f. The comparison of t_{norm} results for different observed time intervals using 70 historical cases is shown in Fig. 17, both with and without considering model uncertainty. After considering both observational and model uncertainties, the number of cases (red scatters) where T_f lies outside the 95 % CI of t_f significantly decreases. For example, for the T_{last}, when only observational uncertainty is considered, 16 cases lie outside the 95 % CI, while after considering model uncertainty, only one case lies outside the 95 % CI. In addition, with the increase in value of m, the number of cases deviating from 95 % CI and the

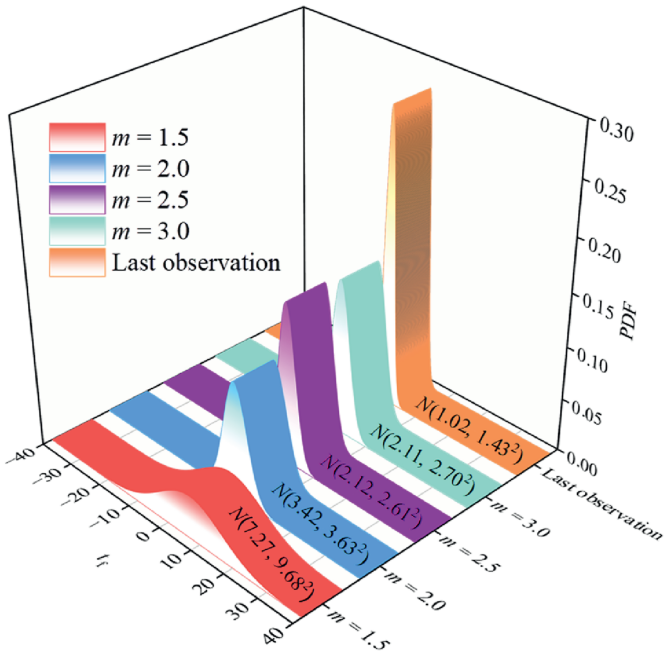

Fig. 15. Normal distribution of model uncertainty for different observed time intervals.

degree of deviation show a decreasing trend on the whole, regardless of whether the model uncertainty is considered.

Furthermore, the study also reveals a negative correlation between A and t_f. The bivariate kernel density contour plot for the joint distribution of A-t_f parameters calculated from the last observation without considering model uncertainty is shown in Fig. 18. The darker region represents a higher density of samples, suggesting a greater probability of the Bayesian-estimated parameters appearing in these regions. The histograms with curves on the top and right sides of the plot represent the sampling distributions of A and t_f, respectively. In the two cases shown in the figures, the negative correlation coefficient ρ between A and t_f is approximately 0.6, despite the prior assumption that A and t_f are independent. Therefore, future studies may consider including the A-t_f joint distribution in Bayesian parameter estimation to provide more accurate inference and facilitate more effective decision-making.

5.2. Explanatory examples of dynamic probabilistic prediction

To incorporate model uncertainty in dynamic prediction, the following predictive strategy is proposed. Assuming the values of m obtained by TDT fall within the intervals (1, 1.5], (1.5, 2], (2, 2.5], (2.5, 3], and (3, $+\infty$] in the dynamic prediction, the model uncertainty terms corresponding to observed time intervals of $T_{1.5}$, T_2, $T_{2.5}$, T_3, and T_{last} are added in the predictive results through Eq. (20). A few explanatory examples of dynamic prediction using three failure cases (Jimingsi landslide, Zhouzhi landslide, and Vajont landslide) outside the database are described as follows.

5.2.1. Jimingsi landslide

Dynamic predictions, with and without including model uncertainty, in the Jimingsi landslide are shown in Fig. 19. According to the BOCD-TDT algorithm, the actual failure time T_f from the identified OA to eventual failure is approximately 91.21 d. Due to the significant TU during the accelerating deformation stage, the inverse velocity curve can be approximately divided into three segments (Fig. 11). Therefore, in the early accelerating deformation stage ($1.1 < m < 1.4$, with a weakly stable trend), it is difficult to obtain a reliable prediction, regardless of whether model uncertainty is considered. With the addition of new monitoring data in the Bayesian model, the predictive accuracy improves, and t_f gradually approaches T_f. When $m > 1.5$, the predictive accuracy is high, and the t_f fluctuates around T_f. When $m > 2$, the deformation trend toward failure becomes evident with extremely high predictive accuracy. When $m > 3$, the landslide deformation exhibits a strongly unstable trend, a deterministic prediction can be carried out in this stage.

By comparing the prediction results with and without considering model uncertainty, it is evident that the prediction interval (FI_{mod}, magenta error bars) considering model uncertainty captures T_f (June 29, 1991) is earlier than the prediction interval (FI_{obs}, blue error bars) without considering model uncertainty. Specifically, the FI_{mod} first includes T_f on May 23, 1991, whereas the FI_{obs} includes T_f for the first time nearly a week later, on May 31, 1991. Moreover, the mean value of t_f (89.39 d) considering model uncertainty approaches T_f on June 2, 1991, and thereafter, the mean value fluctuates around T_f, i.e. the lead time of reliable prediction is 27 d. In contrast, without considering model uncertainty, a reliable prediction is not achieved until June 14, 1991, resulting in a delay of 12 d.

5.2.2. Zhouzhi landslide

Dynamic predictions with and without incorporating model uncertainty in the Zhouzhi landslide are shown in Fig. 20. T_f from the identified OA to the eventual failure is approximately 66.17 d. When $m < 1.5$, the accelerating failure trend is not pronounced, leading to significant fluctuations in the mean and standard deviation of t_f, making it difficult to obtain a reliable prediction. When $m > 1.5$, the predicted mean value gradually converges

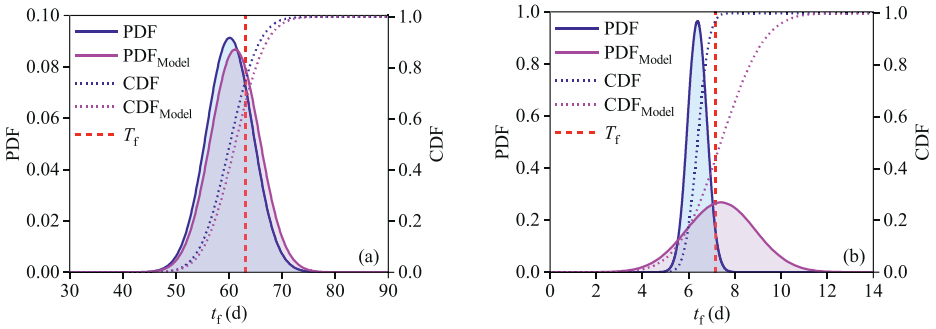

Fig. 16. PDF and CDF of t_f with and without considering the model uncertainty from the last observation in (a) Hogarth landslide (No. 29) and (b) Venetia 2003 failure (No. 64). These two failure cases are from the database. The subscript "Model" represents the distribution function considering model uncertainty.

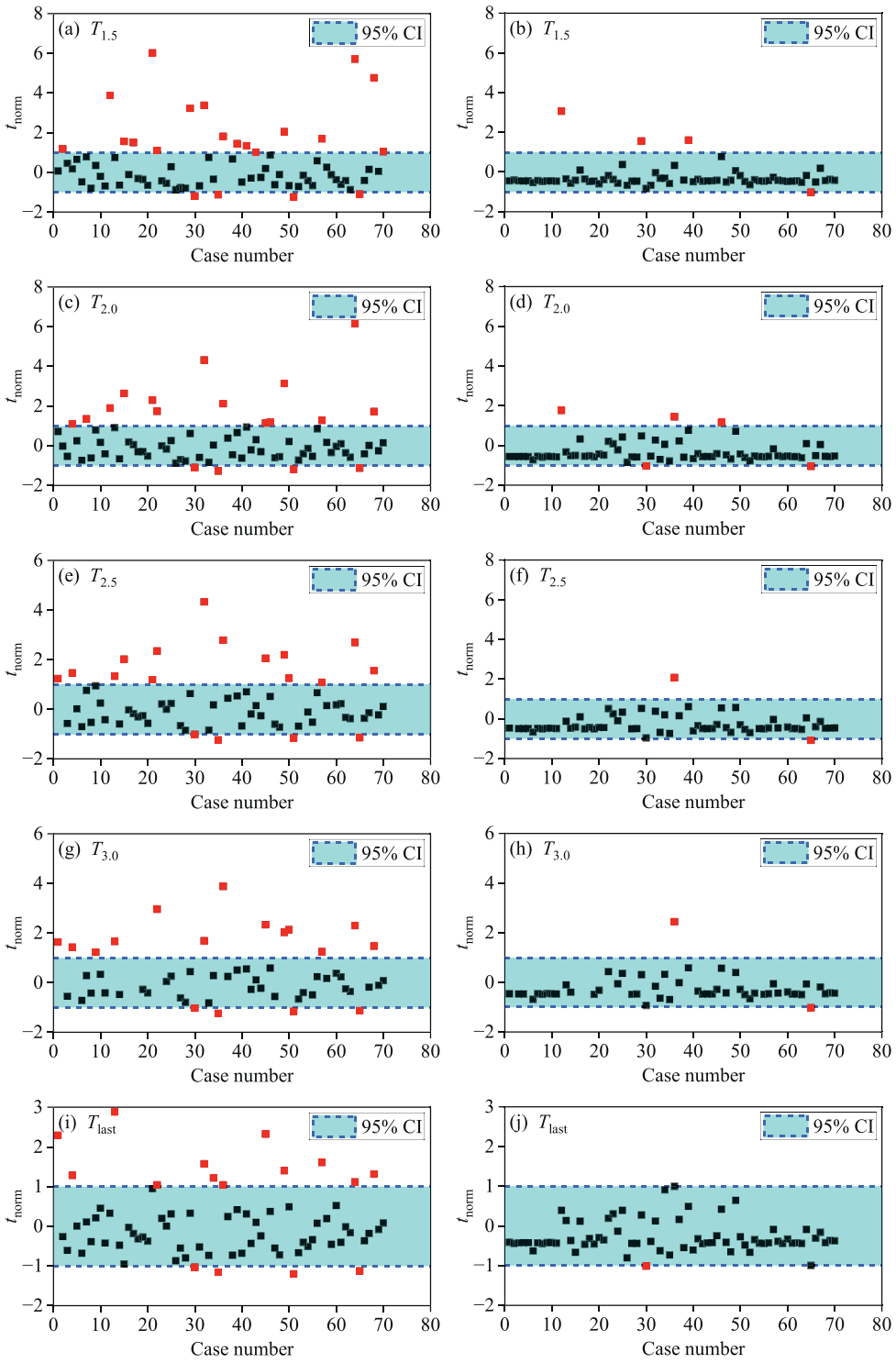

Fig. 17. Comparison of predictive results without (left) and with (right) considering model uncertainty.

toward T_f as m increases, and the prediction interval narrows progressively. Unfortunately, regardless of whether model uncertainty is considered, the LINV method fails to accurately predict the failure, even when the final observation is included in the predictive procedure. Although the LINV method is easy-to-operate and widely used, it does not necessarily imply exceptionally high predictive accuracy (Intrieri et al., 2019), as demonstrated by the calibration of model uncertainty. Additionally, factors such as the dynamic characteristics of the displacement curve and the accuracy of raw data processing have a notable influence on the predictive performance. Using high-frequency monitoring data or multi-data fusion is a feasible solution to address this issue, which will be further analyzed in the Discussion section. Nevertheless, after $m > 1.3$, the prediction interval includes T_f within it.

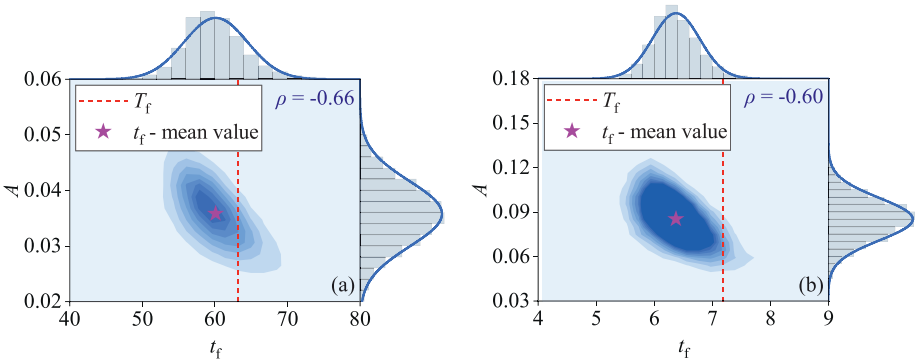

Fig. 18. Joint distributions of t_f and A from the last observation: (a) Hogarth landslide; and (b) Venetia 2003 Failure.

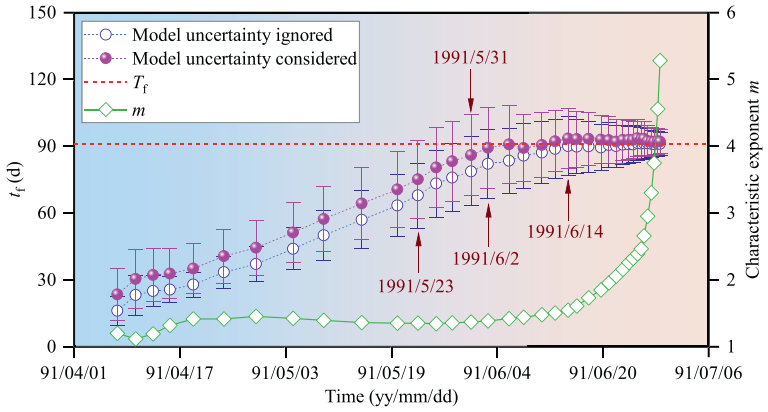

Fig. 19. Comparison of dynamic predictions with and without considering model uncertainty in Jimingsi landslide.

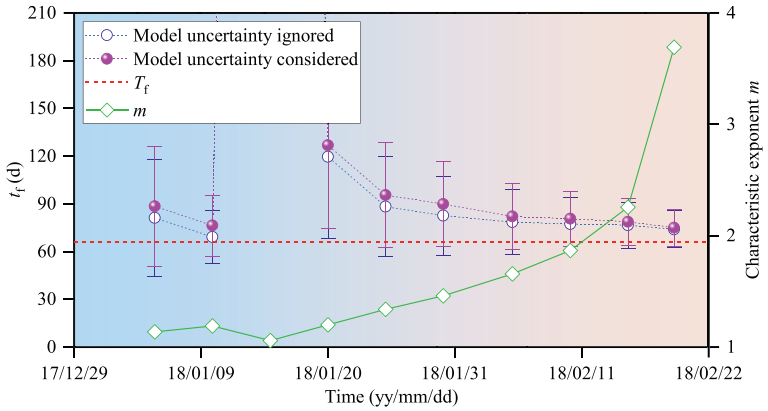

Fig. 20. Comparison of dynamic predictions with and without considering model uncertainty in Zhouzhi landslide.

5.2.3. Vajont landslide

The Vajont landslide experienced three acceleration events (Events 1–3) from the onset of monitoring to its eventual failure, as shown in Fig. 9. The first two acceleration events did not cause catastrophic failure. Dynamic predictions with and without considering model uncertainty for the three acceleration events are shown in Fig. 21. T_f values from the identified OA of the three acceleration events to the eventual failure of the landslide are 1219.94 d, 642.94 d, and 154.42 d, respectively. Similar to the first two failure cases, as m increases, the mean value of t_f tends to stabilize and gradually converges to a certain value. The standard deviation also decreases continuously, leading to a narrowing of the prediction interval. However, the t_f values calculated from Events 1 and 2 differ greatly from T_f. For Event 3, before failure, the obtained mean value of t_f fluctuates around T_f. Excluding individual predictive values, the mean value of t_f calculated with consideration of model uncertainty is closer to T_f than that calculated without considering model uncertainty. The prediction interval considering model uncertainty consistently encompasses T_f throughout the entire calculation process.

For the first two acceleration events, the failure to predict the timing of the catastrophic event occurrence warrants further exploration. In natural environments, many rock slopes typically have intermittent accelerations from initial deformations to

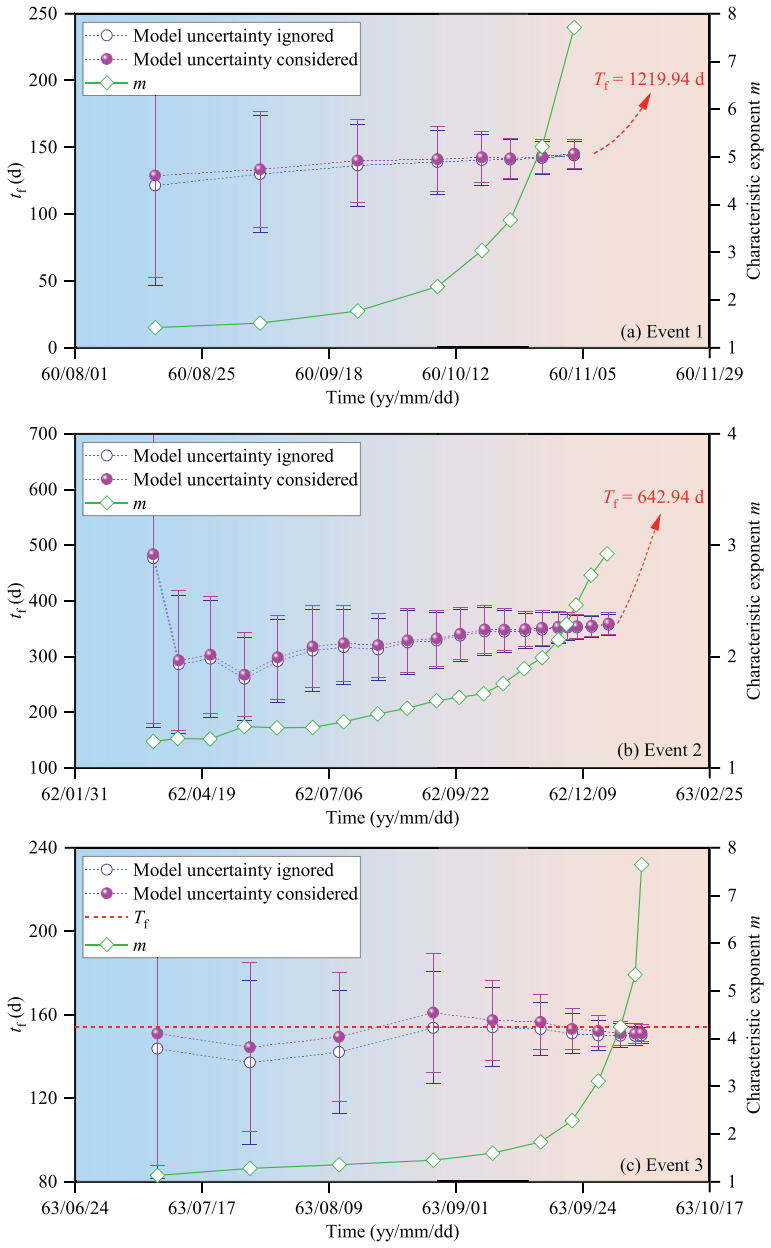

Fig. 21. Comparison of dynamic predictions with and without considering model uncertainty in the Vajont landslide.

catastrophic landslides or collapses. Therefore, it is essential to have a clear understanding of the deformation and failure mechanisms of a slope, along with its current evolutionary stage, for reliable failure prediction. For example, distinguishing whether the slope deformation is due to the creeping of the rock mass or sliding along the sliding surface (or zone) is crucial, as the displacement curves and acceleration patterns may show significant differences between these two types of scenarios. The Vajont landslide is a prehistoric rockslide that was reactivated following reservoir impoundment. Before the reservoir impoundment, the landslide had already developed a deep-seated shear zone with a thickness of 40–50 m, which has a significant influence on the hydrogeological and mechanical behavior of the slope (Paronuzzi et al., 2016). In addition, the materials of the sliding mass have high permeability. Consequently, the landslide deformation is highly sensitive to the strong seepage effect induced by fluctuations in the reservoir water level. In Events 1 and 2, the peak values of the characteristic exponent m are approximately 7.71 and 2.92, respectively. According to the TDT classification, the landslide displacement trends of Events 1 and 2 correspond to substages IIIc (strongly unstable trend) and IIIb (weakly unstable trend). During the first and second impoundment periods, the predictive model is unable to provide a precise t_f. Nevertheless, considering the structural features of the potential sliding mass and its hydrogeological response patterns, proactive and effective emergency measures should be implemented, given the current deformation stage. Moreover, the predictive results of this case demonstrate that utilizing prediction information to develop available prediction criteria or decision-making guidelines is a crucial aspect of failure prediction.

5.3. Impact of SP selection for time-to-failure analysis on prediction reliability

As analyzed above, even if acceleration events are reliably identified, the predictive accuracy remains low, and the predictive

uncertainty is significant due to the relatively obscure failure trend during the initial accelerating deformation stage. Therefore, although OA is crucial for identifying the precursor of failure, the timing for initiating failure prediction requires further evaluation. To clarify this issue, the performance of dynamic prediction is tested using observational data from different SPs within the accelerating deformation stage. The predictive results for the three failure cases (Jimingsi landslide, Zhouzhi landslide, and Vajont landslide), without considering the model uncertainty, are presented in Fig. 22. The observational data following $m > 1.5$ are used, and the changing trend of t_f tends to stabilize; conversely, when SPs before $m < 1.5$ are selected, t_f deviates from T_f and exhibits significant oscillations during the early period. When SPs after $m > 2$ are selected, the predictive accuracy is further enhanced. When SPs after $m > 3$ are selected, a deterministic prediction can be achieved.

Furthermore, the TU during the accelerating deformation stage is another important factor in the selection of SPs. Before discussing the impact of TU on predictions, reliable identification of TU is essential. To this end, an additional detection algorithm for automatically identifying TU points is employed here, namely the piecewise regression model with Bayesian information criterion (PRM-BIC) proposed by Pilgrim (2021). A more detailed description of PRM-BIC can be found in the original literature. Taking the Jimingsi landslide as an example, TU identification and segmented dynamic prediction are shown in Fig. 23. According to this algorithm, two TU points are identified in this landslide, dividing the Λ-t curve into three segments (Trends 1–3). The identified positions of the TU points are reasonable and objectively reflect the changing characteristics of the Λ-t curve. Using the observational data from Trends 1 and 2, the prediction errors are relatively large. In comparison, the prediction errors for Trend 3 are relatively small, and t_f becomes more stable over time, as expected.

In summary, selected SPs and TU points have varying degrees of influence on the reliability of dynamic predictions. While using subsequent observational data following the OA for time-to-failure analysis, TU identification should also be conducted for the continuously added new observations. When a TU point occurs, it is recommended to use it as the SP for calculations and update subsequent predictions accordingly. At the same time, multiple time-to-failure analyses should be implemented, updating predictions from different SPs to provide more comprehensive predictive information. Using observational data with $m > 2$ for failure prediction is a better selection.

6. Discussion

6.1. Decision-making criteria for imminent failure in dynamic prediction

The above analyses indicate that the LINV method used in the dynamic analysis has clearly defined stage-dependent characteristics and uncertainties, making it highly challenging to accurately predict the precise timing of slope failure. Therefore, rather than focusing solely on achieving extremely high levels of predictive accuracy, an alternative way is to explore how to use predictive information to make reliable decisions. To this end, the following decision-making suggestions are proposed.

It is essential to first identify the deformation stages of rock slopes, thereby determining the appropriate timing for initiating the time-to-failure analysis. (1) In the initial and steady deformation stages, slope deformation develops relatively slowly, with no clear indicators of imminent failure, making it difficult to accurately predict the slope failure time. Therefore, during these two stages, emphasis should be placed on identifying slope deformation stages and then early detection of any potential accelerating deformation behavior. The BOCD-TDT algorithm provides an effective method for the division of deformation stages and the identification of acceleration events online. (2) During the initial accelerating deformation stage, the failure trend is not yet clearly defined since the time from T_f is relatively far off. As a result, even small disturbances can lead to significant prediction errors. In this period, it is recommended to integrate various observed information, such as macroscopic slope deformation characteristics, and focus on predicting the failure trend to assess the possibility of slope failure. (3) Once $m > 1.5$, a concrete time-to-failure analysis can be initiated. When $m > 2$, a relatively reliable prediction for failure time can be made. When $m > 3$, a deterministic prediction for failure time is possible. The predicted mean value and prediction interval can be used to assess the most likely time of slope failure.

For the case of $m > 1.5$, a failure probability criterion is provided here to quantify the risk arising from predictive uncertainty, which combines t_f with the failure probability P_f:

$$P_f\left(T_f < \tau\right) = \Phi\left(\frac{\tau - \mu_f - \mu_m}{\sqrt{\sigma_f^2 + \sigma_m^2}}\right) \tag{12}$$

where τ is the assumed slope failure time, and $\tau = t_p + \Delta t$, in which t_p is the present observed time, and Δt is the time interval between τ and t_p. Eq. (12) expresses that the P_f of slope failure occurring is given by $\Phi(\bullet)$ within the future Δt. The value of Δt can be selected based on the specific situation and the risk attitude of decision-makers. In this study, in conjunction with the stage division of the accelerating deformation stage, the following prediction criteria are preliminarily established:

$$\left.\begin{array}{l} P_f \geq 50\% \ (m \geq 1.5, \Delta t = 14\text{d}) \\ P_f \geq 25\% \ (m \geq 2, \Delta t = 7\text{d}) \\ P_f \geq 5\% \quad (m \geq 3, \Delta t = 1\text{d}) \end{array}\right\} \tag{13}$$

According to Eq. (13), when $m \geq m'$ (e.g. 1.5), the imminent failure signal of a slope can be issued if $P_f \geq P_f'$ within the future Δt (e.g. 14 d). The selection of Δt as 1-, 7-, and 14-d in Eq. (13) is inspired by Crosta and Agliardi (2003), and it also allows for sufficient lead time to respond to risk scenarios of varying intensities. Similarly, the gradation of P_f levels considers the deformation characteristics of creep rock slopes and refers to existing studies on hazard risk assessment (Chowdhury and Flentje, 2003; Chen et al., 2022). Overall, the selection of these parameter values is consistent with the evolutionary process of creeping rock slopes and human risk perception habits.

The calculated results for validating the feasibility of the proposed prediction criteria are shown in Fig. 24, using three failure cases of Jimingsi landslide, Zhouzhi landslide, and Vajont landslide. Based on Eq. (13), the red shaded area represents the critical prediction zone where imminent failure can be predicted, while the blue shaded area indicates a non-prediction zone where a reliable prediction cannot yet be made. In the Jimingsi landslide, when $m > 1.5$, the P_f of slope failure occurring within the next 14 d exceeds 80 %, and thereafter, with the increase in value of m, the P_f remains no lower than 50 %. In the Zhouzhi landslide, a reliable prediction signal for imminent failure can only be issued when $m > 2$, with the corresponding P_f being 25.4 %, which can be issued about 4 d in advance. In the Vajont landslide, a reliable prediction for imminent failure cannot be made until $m > 3$, corresponding to a P_f of 9.4 %, but this allows for a warning approximately 13 d in advance. The three case studies validate the feasibility of the proposed prediction criteria. Overall, a reliable prediction for

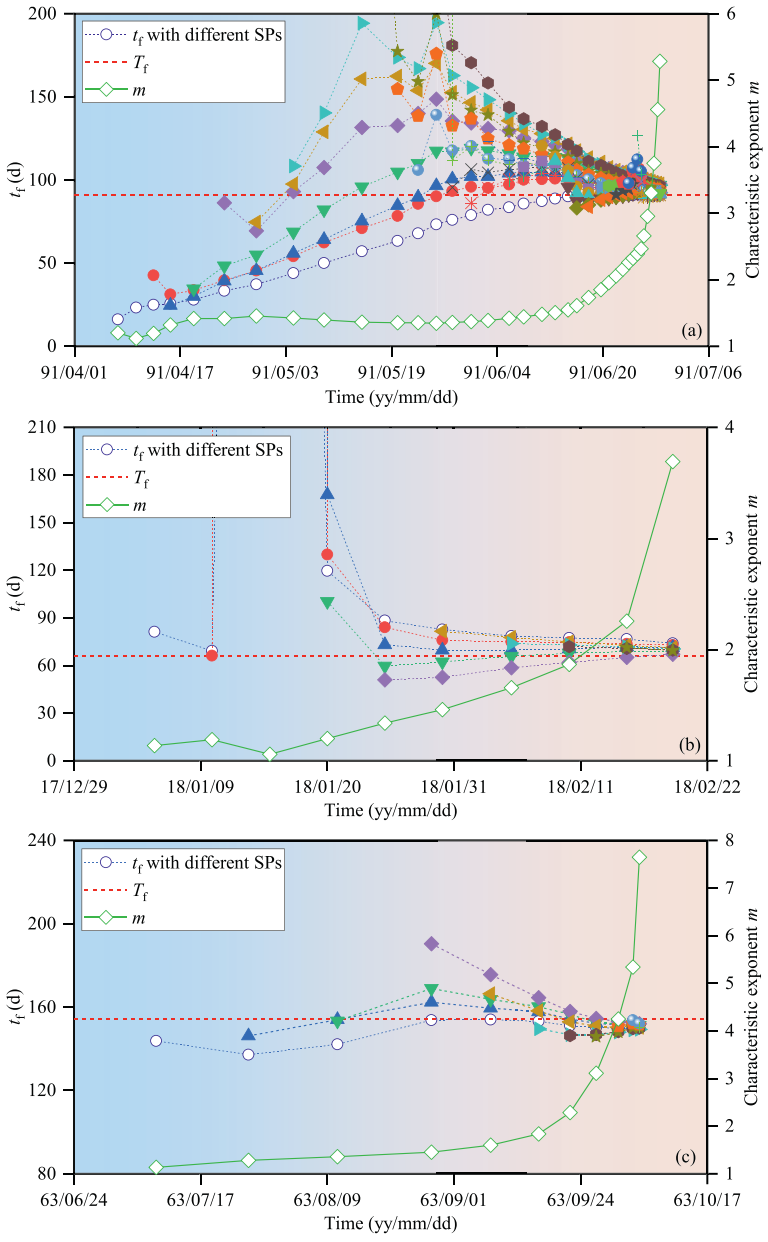

Fig. 22. Mean values of t_f without considering model uncertainty obtained from different SPs: (a) Jimingsi landslide; (b) Zhouzhi landslide; and (c) Vajont landslide.

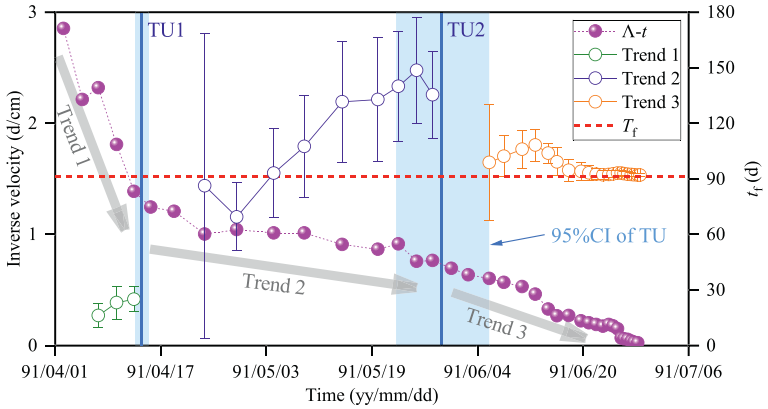

Fig. 23. TU identification using the PRM-BIC algorithm and segmented prediction in Jimingsi landslide. The blue shaded area in the figure represents the uncertainty in TU identification, represented by a 95 % CI.

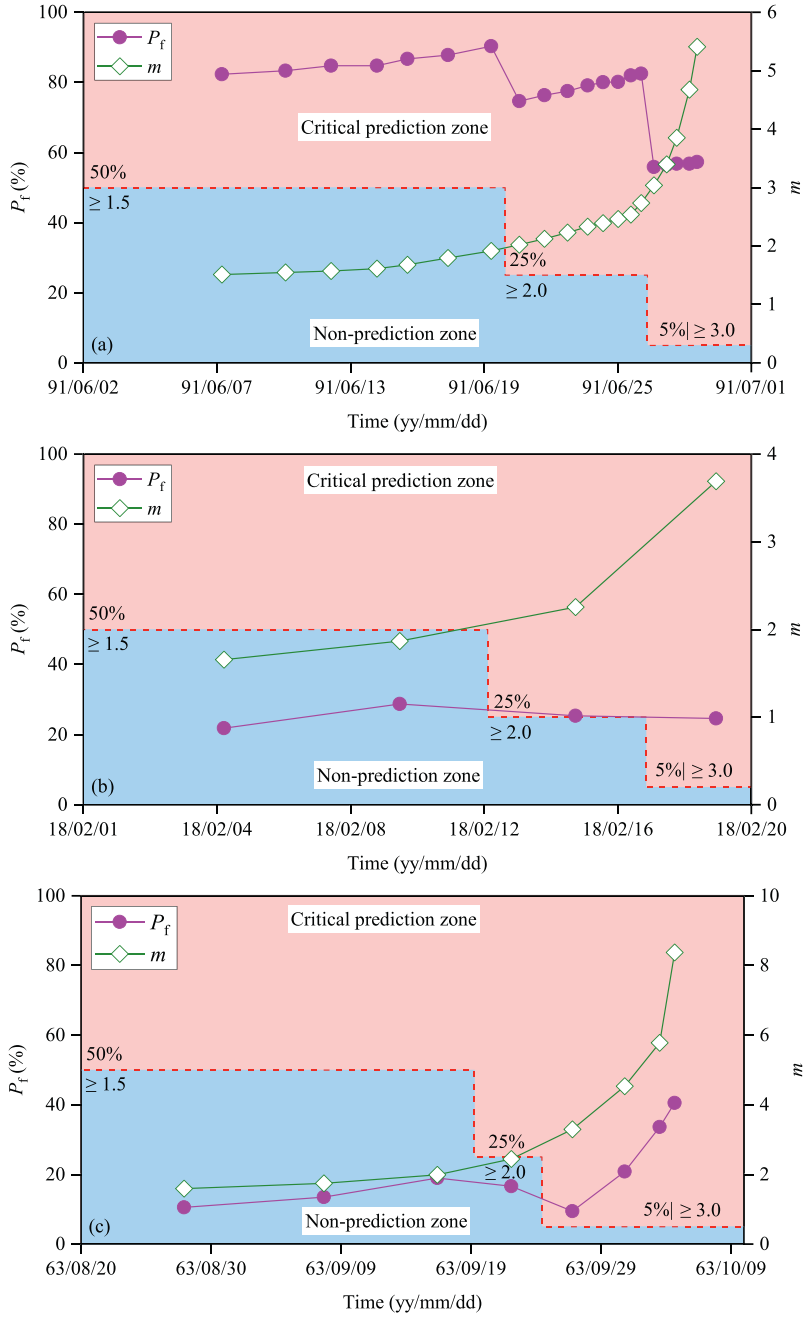

Fig. 24. Probabilistic decision of imminent failure: (a) Jimingsi landslide; (b) Zhouzhi landslide; and (c) Vajont landslide.

imminent failure can be made only when $m > 2$, which is consistent with the analysis results discussed earlier.

6.2. A decision-making framework for failure prediction through multi-data fusion

Previous studies have generally overlooked how to organically integrate predictive information from multiple monitoring points for time-to-failure analysis. They either relied solely on data from a single monitoring point for time-to-failure analysis or only provided qualitative descriptions of the predictive information obtained from multiple monitoring points, lacking quantitative decision-making methods (Rose and Hungr, 2007; Carlà et al., 2017b; Silva et al., 2021). In this study, a conceptual framework for multi-source predictive information fusion is provided, along with a preliminary exploration of its application for predictive decisions.

The conceptual framework for multi-source information fusion in slope failure prediction is illustrated in Fig. 25. The specific implementation process is as follows:

(1) Deformation zone partition. Due to the spatial variability of materials and structure in rock slopes, especially large-scale rock slopes, the deformation intensity and processes of different zones within the same slope vary, and even exhibit entirely different deformation patterns (Crosta et al., 2017). Therefore, potential failure zones of the slope should be divided into multiple sub-zones according to the geological conditions, the spatial layout of monitoring points, and the

deformation patterns reflected by monitoring data. Accordingly, monitoring points should be grouped.

(2) Online accelerating precursor identification using multi-data. Identifying accelerating precursors is the basis for conducting time-to-failure analysis. As previously mentioned, due to the spatio-temporal variability in the evolution of rock slopes and the presence of outliers in individual monitoring data, relying solely on single monitoring data for accelerating precursor identification is not always effective. Therefore, the proposed BOCD-TDT algorithm should be extended to utilize multi-source monitoring data for OA identification. This requires further research in the future.

(3) Time-to-failure analysis and selection of optimal fusion targets. The time-to-failure analysis should be performed on the observational information obtained from different monitoring points belonging to different sub-zones. Generally, when a slope failure is imminent, the deformation in the failure zone exhibits a synchronization effect (Lin et al., 2013). Therefore, before data fusion, an available selection criterion or threshold (e.g. Bayesian decision-making criteria, clustering analysis method, and machine learning method) should be applied to filter the predictive information obtained from monitoring points, to determine the optimal number of fusion targets.

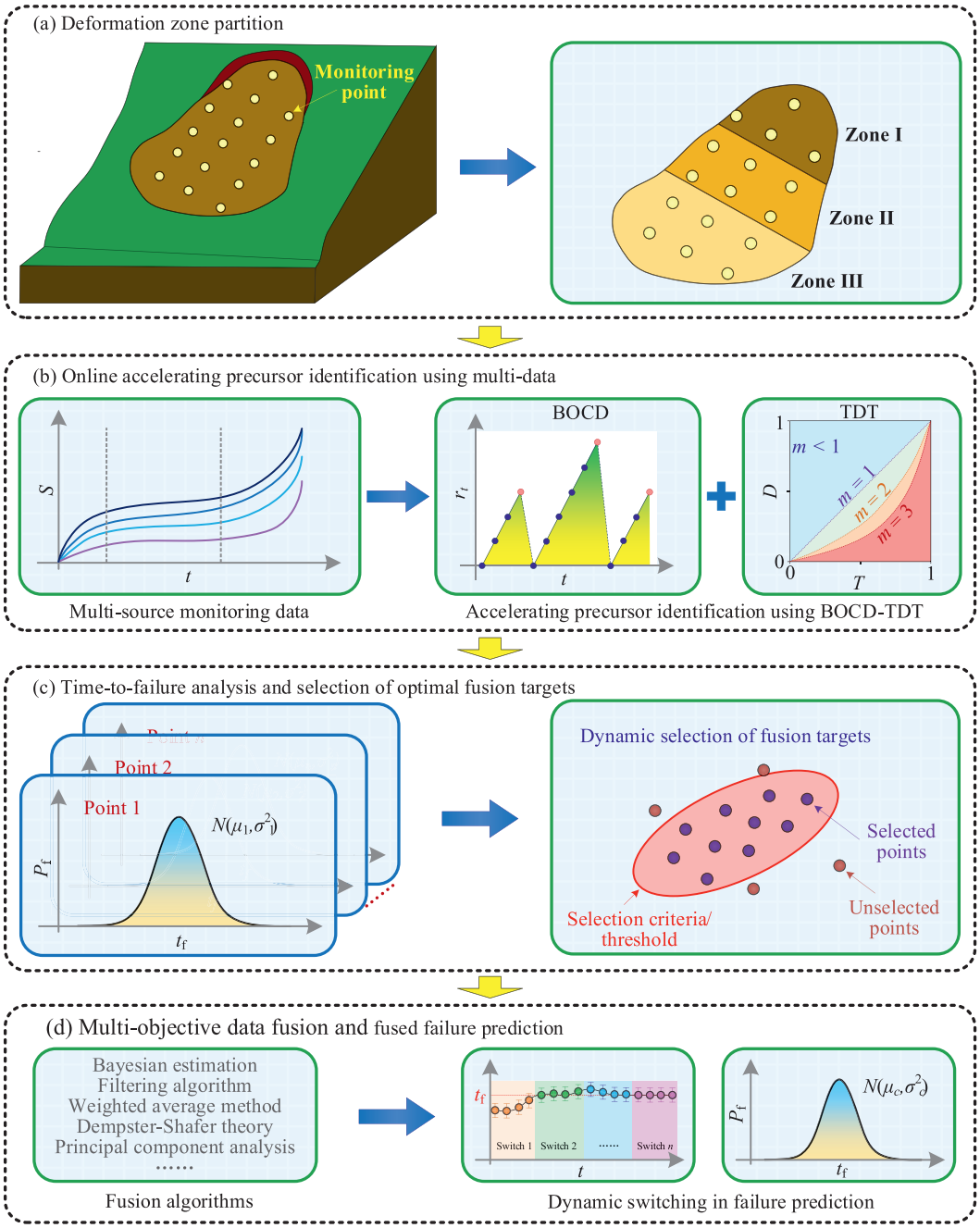

Fig. 25. A conceptual framework of multi-source information fusion for slope failure prediction.

(4) Multi-objective data fusion and fused failure prediction. Multi-objective fusion of the predictive information is performed using fusion algorithms such as Bayesian estimation and filtering algorithms. During the data fusion process, the selection of the optimal number of fusion points should be performed simultaneously, allowing for dynamic switching of the fused monitoring targets. This dynamic switching is based on the online selection results of the optimal fusion targets.

A simple demonstration of fusion prediction using multi-source data is presented using the observational data obtained from two monitoring points of the Zhouzhi landslide, as shown in Fig. 26. Since there are only two monitoring points, the step of selecting the optimal number of fusion points is omitted. The fusion algorithm also adopts the relatively simple Kalman filter (Welch and Bishop, 1995), which is actually a special case of Bayesian estimation. For the fusion of k data points following $N(\mu_k, \sigma_k^2)$ using the Kalman filter, the fused mean μ_{fused} and standard deviation σ_{fused} can be derived as follows:

$$\left.\begin{aligned}\mu_{\text{fused}} &= \sum_{i=1}^{K}\frac{\mu_k}{\sigma_k^2}\Big/\sum_{i=1}^{k}\frac{1}{\sigma_i^2}\\ \sigma_{\text{fused}} &= \sqrt{\left(\sum_{i=1}^{k}\frac{1}{\sigma_i^2}\right)^{-1}}\end{aligned}\right\} \tag{14}$$

The derivation process of the multi-data fusion method using the Kalman filter is described in Appendix D. From the above equation, it can be observed that as the variance of t_f at a given observation point increases, its weight in data fusion decreases. The t_f calculated at monitoring point JC03 is very close to T_f, with a smaller standard deviation than that at JC02 (Fig. 26b), making the fused prediction closer to the predictive result of JC03. Compared to predictions only using JC02 or JC03, the fused prediction yields better results in this case, with t_f exhibiting more stable changes over time. Therefore, it is strongly recommended that failure prediction involve multivariate fusion analysis to avoid significant bias caused by the inappropriate selection of a single monitoring point.

6.3. Applicability and limits of the proposed methods

This study proposes the use of Bayesian inference to detect accelerating precursors and predict failure time for rock slopes, and validates the feasibility and effectiveness of the proposed methods. However, the applicability and limitations of the method need to be clarified, as detailed below:

(1) The proposed methods are more suitable for rock slopes with creep deformation characteristics, but they also show promising application potential in brittle failure-type rock slopes. Previous studies have demonstrated that high-frequency monitoring data can significantly improve the identification of accelerating precursors of brittle failures and extend the application scope of the LINV method (Carlà et al., 2017a). To preliminarily assess the feasibility of the BOCD-TDT algorithm for OA detection, a brittle failure case with high-frequency monitoring data is used, as detailed in Appendix E. Due to the sudden and rapid nature of brittle failure, it is suggested that the changepoint signals detected by the BOCD algorithm can be directly used as early-warning signals. For similar reasons, probabilistic failure prediction may be conducted without considering model uncertainty.

(2) In the BOCD-TDT algorithm, the same timescale λ and prior hyperparameters μ_0, κ_0, α_0, and β_0 are used in all cases for convenience, and good detection results are achieved. However, it must be emphasized that these parameters should be calibrated based on the specific scenarios due to differences in data sources, monitoring instrument accuracy, sampling frequency, and other factors. As an example, this study also evaluated the performance of changepoint detection under different λ values, as detailed in Appendix F. The results demonstrate that the changepoint detection results obtained from different λ values indeed vary considerably. Therefore, in specific cases, the timescale and hyperparameters should be calibrated or adaptively adjusted based on the detection results from preliminary monitoring data. Additionally, it is worth noting that, compared to other λ values, the parameter ($\lambda = 100$) used in the three landslide cases presented in this study yields optimal results.

(3) As mentioned above, high-frequency monitoring data should be used whenever possible to improve the ability of the proposed methods to identify accelerating precursors and predict failure time. A crucial prerequisite is that the noise in the high-frequency monitoring data must be scientifically processed (Sharifi et al., 2022). Furthermore, with the widespread application of technologies such as interferometric synthetic aperture radar (InSAR) in slope

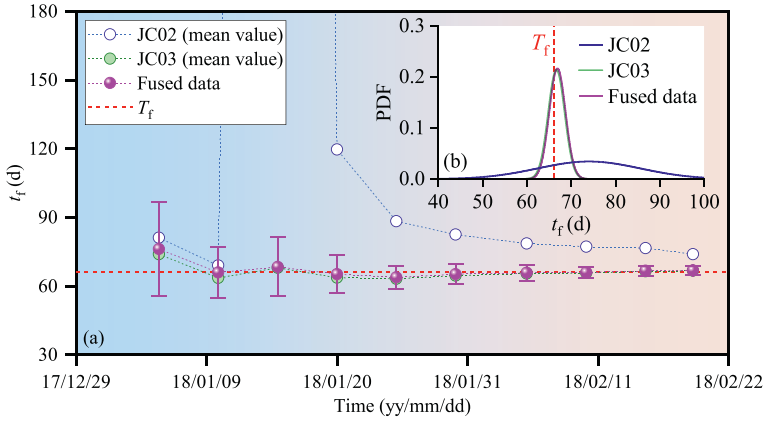

Fig. 26. Time-to-failure fusion analysis in Zhouzhi landslide. (a) Dynamic prediction; and (b) PDF of t_f obtained from the last observation.

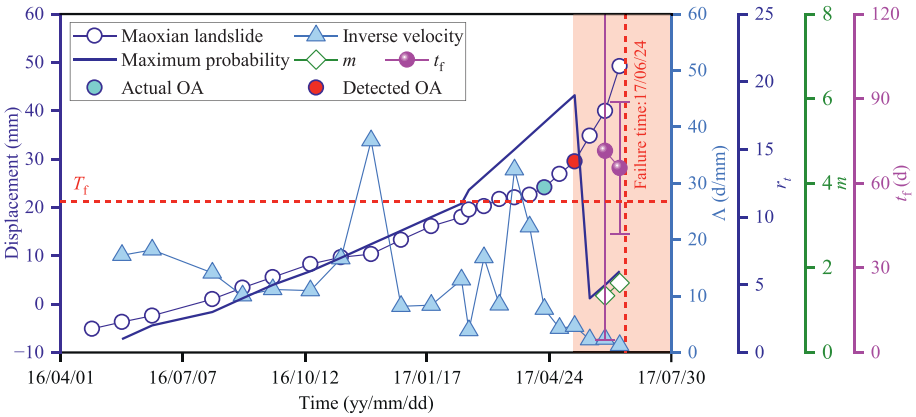

Fig. 27. Accelerating precursor identification and failure prediction using InSAR data in Maoxian landslide.

monitoring, there is growing interest in using such low-sampling frequency and relatively low-precision monitoring data for failure prediction (Li et al., 2020). The results of the accelerating precursor and failure prediction using InSAR data in the Maoxian landslide are shown in Fig. 27 (Yan, 2021). The proposed methods can detect its accelerating precursor, and the prediction interval can also encompass T_f, but the accuracy is relatively poor. However, InSAR monitoring offers several advantages, including non-contact measurement, large-scale coverage, multi-temporal analysis, low cost, data visualization, and adaptability to harsh environments (Casagli et al., 2023; Zhu et al., 2024). These capabilities make InSAR suitable for long-term, spatially extensive monitoring of potentially unstable slopes, particularly in areas that are difficult to access. The 2008 Wenchuan earthquake prompted substantial investment by the Chinese government in early-warning systems of geological disasters. China is currently constructing a nationwide monitoring system from the perspectives of "space–air–ground–interior" and "multi-source, multi-scale, and multi-physical field" (Ji et al., 2019; Xu et al., 2023; Zhu et al., 2024). This initiative has further elevated the importance of InSAR monitoring, accelerating progress toward the established goals for the early-warning systems of unstable slopes, which are to provide timely, comprehensive, and accurate alerts. Therefore, as a crucial component of early-warning systems, the predictive information provided by InSAR remains a valuable reference for the early warning of slope creep failure, especially in large-scale rock slopes.

(4) As an accelerating precursor phenomenon generally exists before slope failure, the methods of precursor identification and dynamic probabilistic prediction proposed in this study, while primarily applicable to rock slopes, can also be extended for failure prediction and early warning of soil slope failures. Additionally, the proposed methods can be applied to non-displacement monitoring data, such as microseismic signals and tilting angle of deformation (Amitrano et al., 2005; Xie et al., 2020; Wang et al., 2025), as long as such monitoring data can capture the power-law growth trend of slope deformation before failure. For example, the feasibility of the proposed methods using tilting angle data from the Heifangtai soil landslide is shown in Fig. 28 (Wang et al., 2022). However, if the proposed methods are to be extended to soil slopes and non-displacement monitoring data, further case studies are required to calibrate model parameters (e.g. timescale, hyperparameters, and model uncertainty).

(5) Rock slope material failure involves a positive feedback mechanism during the accelerating deformation stage, leading to countless doubling operations in deformations until eventual failure (Sammis and Sornette, 2002; Chen and Jiang, 2020). This process typically results in a power-law form for the velocity–time curves of the accelerating deformation stage. The curve shape of the inverse velocity

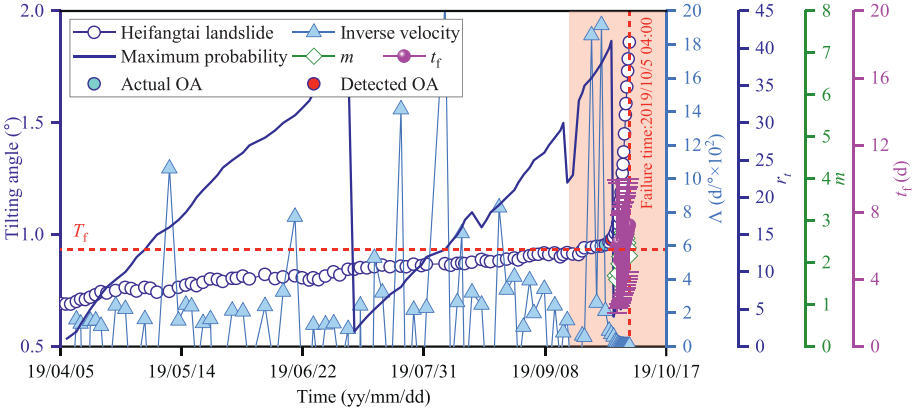

Fig. 28. Accelerating precursor identification and failure prediction using tilting angle data in Heifangtai landslide.

trend is related to the properties of the underlying physical mechanisms driving instability, particularly when the stress transfer processes during crack nucleation and propagation dominate, which are consid]ered to exhibit a linear failure trend (Kilburn and Petley, 2003; Carlà et al., 2018; Zheng et al., 2024a, 2024b). In future research, physical-mechanical mechanisms, heterogeneity of materials, and drivers of instability should be incorporated into the INV method for time-to-failure analysis to provide more convincing predictive results.

(6) Identification of OA and failure probability criterion can be used to set dynamic thresholds for the early-warning procedure. The occurrence of OA is considered the initial alert threshold, signaling the start of a progressive stage of failure (Carlà et al., 2017b), which simultaneously triggers the activation of the probabilistic failure prediction procedure. The failure probability criterion can serve as a secondary alert threshold or an ultimate alert threshold to identify the potential risk of slope failure in advance and implement predetermined evacuation and/or remedial strategies promptly.

(7) The methods proposed in this study do not provide a universal tool for failure predictions of all types of rock slopes under all circumstances, due to the complex deformation process and failure mechanisms. The integration of geological knowledge (e.g. material properties, rock mass structures, hydrology, and macroscopic deformation characteristics), multi-source and multi-scale monitoring data, and mathematical (or numerical) models is likely the essential path for future slope deformation and failure predictions. With the rapid development of machine learning, physics-informed and data-driven failure time prediction models are expected to become a powerful tool (Cui et al., 2024; Liu et al., 2024). Nevertheless, the results of this study suggest that incorporating the proposed methods into the early-warning procedures of rock slopes would be of significant value.

7. Conclusions

In this study, the BOCD-TDT algorithm for online identification of kinetic behaviors and accelerating precursors is proposed and validated using failure cases characterized by different deformation patterns of rock slopes. Bayesian estimation is then used to conduct dynamic probabilistic failure prediction, which can provide predictive decision criteria and recommendations. The following conclusions can be drawn from the main results:

(1) The BOCD-TDT algorithm can divide the kinetic behaviors of different deformation stages for three types of creep deformation patterns of rock slopes online. It can also reliably identify the accelerating precursor phenomena and the corresponding onset of acceleration. The detection results show that the BOCD-TDT algorithm is highly sensitive to inverse velocity–time series. Therefore, it is recommended to use inverse velocity data for precursor identification.

(2) The uncertainty calibration results indicate significant differences in model uncertainty across different accelerating deformation substages. With the development of slope deformation, both the mean and standard deviation of model uncertainty show an overall trend of gradual decrease. When the characteristic exponent $m > 2$ of slope deformation, a reliable failure prediction can be achieved. Only when the characteristic exponent $m > 3$ is observed can the deterministic prediction yield ideal results.

(3) Predictive reliability can be enhanced by dynamically superimposing the corresponding observational and model uncertainties according to the changes in slope deformation stages. In light of the significant TU detected, it is advisable to adjust the SP of the predictive procedure to coincide with the TU point. Additionally, multi-data fusion can reduce the uncertainty in failure prediction caused by the improper selection of individual monitoring points, thereby enhancing predictive accuracy.

(4) The case study validates the feasibility of the proposed quantitative criterion for slope failure prediction combined with predicted failure time and failure probability, which can provide a valuable reference for the early warning of slope disasters.

CRediT authorship contribution statement

Mingxi Chen: Writing – original draft, Resources, Methodology, Funding acquisition, Conceptualization. **Zihan Fu:** Visualization. **Feng Xiong:** Validation. **Jie Jiang:** Supervision. **Qinghui Jiang:** Writing – review & editing.

Declaration of competing interest

The authors declare that they have no known competing financial interests or personal relationships that could have appeared to influence the work reported in this paper.

Acknowledgements

The authors acknowledge the financial support from the Major Project of Guangxi Science and Technology (Grant No. AA23023016), Guangxi Science and Technology Base and Talent Special Project (Grant No. AD23026111), and Guangxi Natural Science Foundation (Grant No. 2024GXNSFBA010226). The authors also express special thanks to the editors and anonymous reviewers for their constructive comments.

Appendice A–F Supplementary data

Supplementary data to this article can be found online at https://doi.org/10.1016/j.jrmge.2025.08.048.

References

Abdulai, M., Sharifzadeh, M., 2019. Uncertainty and reliability analysis of open pit rock slopes: a critical review of methods of analysis. Geotech. Geol. Eng. 37 (3), 1223–1247.

Adams, R., MacKay, D., 2007. Bayesian online changepoint detection. https://doi.org/10.48550/arXiv.0710.3742.

Agliardi, F., Scuderi, M., Fusi, N., Collettini, C., 2020. Slow-to-fast transition of giant creeping rockslides modulated by undrained loading in basal shear zones. Nat. Commun. 11 (1), 1352.

Amitrano, D., Grasso, J., Senfaute, G., 2005. Seismic precursory patterns before a cliff collapse and critical point phenomena. Geophys. Res. Lett. 32 (8). https://doi.org/10.1029/2004GL022270.

Bak, M., Bak, K., Szubert, M., Welc, E., 2019. The area affected by sturzstrom in the Friulian dolomites as the place to learn and understand the strength of natural forces and consequences for the natural environment and local communities. Acta Geotur 10 (1), 40–50.

Blondeau, S., Gunnell, Y., Jarman, D., 2021. Rock slope failure in the Western alps: a first comprehensive inventory and spatial analysis. Geomorphology 380, 107622.

Boué, A., Lesage, P., Cortés, G., Valette, B., Reyes Dávila, G., 2015. Real-time eruption forecasting using the material failure forecast method with a Bayesian approach. J. Geophys. Res. Solid Earth 120 (4), 2143–2161.

Bozzano, F., Cipriani, I., Mazzanti, P., Prestininzi, A., 2014. A field experiment for calibrating landslide time-of-failure prediction functions. Int. J. Rock Mech. Min. Sci. 67, 69–77.

Carlà, T., Farina, P., Intrieri, E., Botsialas, K., Casagli, N., 2017a. On the monitoring

and early-warning of brittle slope failures in hard rock masses: examples from an open-pit mine. Eng. Geol. 228, 71–81.
Carlà, T., Intrieri, E., Di Traglia, F., Nolesini, T., Gigli, G., Casagli, N., 2017b. Guidelines on the use of inverse velocity method as a tool for setting alarm thresholds and forecasting landslides and structure collapses. Landslides 14 (2), 517–534.
Carlà, T., Macciotta, R., Hendry, M., et al., 2018. Displacement of a landslide retaining wall and application of an enhanced failure forecasting approach. Landslides 15 (3), 489–505.
Casagli, N., Intrieri, E., Tofani, V., Gigli, G., Raspini, F., 2023. Landslide detection, monitoring and prediction with remote-sensing techniques. Nat. Rev. Earth Environ. 4 (1), 51–64.
Cascini, L., Calvello, M., Grimaldi, G., 2014. Displacement trends of slow-moving landslides: classification and forecasting. J. Mt. Sci. 11 (3), 592–606.
Cascini, L., Scoppettuolo, M., Babilio, E., 2022. Forecasting the landslide evolution: from theory to practice. Landslides 19 (12), 2839–2851.
Chen, L., Zhang, W., Paneiro, G., He, Y., Hong, L., 2024a. Efficient numerical-simulation-based slope reliability analysis considering spatial variability. Acta Geotech. 19 (5), 2691–2713.
Chen, M., Feng, A., Wei, W., Jiang, Q., 2024b. Statistical analysis of long-term deformations and determination of warning thresholds for near-dam reservoir bank slopes. Bull. Eng. Geol. Environ. 83 (11), 437.
Chen, M., Jiang, Q., 2020. An early warning system integrating time-of-failure analysis and alert procedure for slope failures. Eng. Geol. 272, 105629.
Chen, M., Wei, W., Jiang, Q., 2022. Use of quantile regression with fukui-okubo model for prediction and early warning of reservoir bank slope failure. Rock Mech. Rock Eng. 55 (11), 7145–7169.
Chowdhury, R., Flentje, P., 2003. Role of slope reliability analysis in landslide risk management. Bull. Eng. Geol. Environ. 62, 41–46.
Crosta, G., Agliardi, F., 2003. Failure forecast for large rock slides by surface displacement measurements. Can. Geotech. J. 40 (1), 176–191.
Crosta, G., Agliardi, F., Rivolta, C., Alberti, S., Dei Cas, L., 2017. Long-term evolution and early warning strategies for complex rockslides by real-time monitoring. Landslides 14 (5), 1615–1632.
Cui, H., Medina, V., Hürlimann, M., Ji, J., 2024. Fast physically-based probabilistic modelling of rainfall-induced shallow landslide susceptibility at the regional scale considering geotechnical uncertainties and different hydrological conditions. Comput. Geotech. 172, 106400.
Dick, G., Eberhardt, E., Cabrejo-Liévano, A., Stead, D., Rose, N., 2015. Development of an early-warning time-of-failure analysis methodology for open-pit mine slopes utilizing ground-based slope stability radar monitoring data. Can. Geotech. J. 52 (4), 515–529.
Donati, D., Stead, D., Brideau, M., Ghirotti, M., 2021. Using pre-failure and post-failure remote sensing data to constrain the three-dimensional numerical model of a large rock slope failure. Landslides 18 (3), 827–847.
Du, H., Song, D., 2022. Investigation of failure prediction of open-pit coal mine landslides containing complex geological structures using the inverse velocity method. Nat. Hazards 111 (3), 2819–2854.
Evans, S., 2006. The formation and failure of landslide dams: an approach to risk assessment. Ital. J. Eng. Geol. Environ. 1, 15–20.
Fearnhead, P., 2006. Exact and efficient Bayesian inference for multiple change-point problems. Stat. Comput. 16 (2), 203–213.
Fell, R., Hungr, O., Leroueil, S., Riemer, W., 2000. Keynote lecture – geotechnical engineering of the stability of natural slopes, and cuts and fills in soil. In: ISRM International Symposium (ISRM 2000). Melbourne, Australia. Paper No. ISRM-IS-2000-002.
Fukuzono, T., 1985. A method to predict the time of slope failure caused by rainfall using the inverse number of velocity of surface displacement. In: Proceedings of the 4th International Conference and Field Workshop on Landslides, pp. 145–150. Tokyo, Japan.
Gu, X., Wang, L., Ou, Q., Zhang, W., Sun, G., 2023. Reliability assessment of rainfall-induced slope stability using Chebyshev-Galerkin-KL expansion and Bayesian approach. Can. Geotech. J. 60 (12), 1909–1922.
Gu, X., Zhang, W., Ou, Q., Zhu, X., Qin, C., 2024. Conditional random field-based stochastic analysis of unsaturated slope stability combining Hoffman method and Bayesian updating. Eng. Geol. 330, 107415.
Hastings, W., 1970. Monte Carlo sampling methods using Markov chains and their applications. Biometrika 57 (1), 97–109.
Hu, Y., Sun, Z., Ji, J., 2024. Pseudo-dynamic stability analysis of 3D rock slopes considering tensile strength-modified Hoek–Brown failure criterion: seismic UBLA implementations. Eng. Geol. 343, 107786.
Intrieri, E., Carlà, T., Gigli, G., 2019. Forecasting the time of failure of landslides at slope-scale: a literature review. Earth Sci. Rev. 193, 333–349.
Intrieri, E., Gigli, G., 2016. Landslide forecasting and factors influencing predictability. Nat. Hazards Earth Syst. Sci. 16 (12), 2501–2510.
Ji, J., Gao, Y., Lü, Q., Wu, Z., Zhang, W., Zhang, C., 2019. China's early warning system progress. Science 365 (6451), 332–332.
Jiang, S., Li, D., Zhang, L., Zhou, C., 2014. Time-dependent system reliability of anchored rock slopes considering rock bolt corrosion effect. Eng. Geol. 175, 1–8.
Kilburn, C., Petley, D., 2003. Forecasting giant, catastrophic slope collapse: lessons from Vajont, northern Italy. Geomorphology 54 (1–2), 21–32.
Lau, Y., Wang, K., Wang, Y., et al., 2023. Monitoring of rainfall-induced landslides at Songmao and Lushan, Taiwan, using IoT and big data-based monitoring system. Landslides 20 (2), 271–296.
Li, M., Zhang, L., Ding, C., Li, W., Luo, H., Liao, M., Xu, Q., 2020. Retrieval of historical surface displacements of the Baige landslide from time-series SAR observations for retrospective analysis of the collapse event. Remote Sens. Environ. 240, 111695.
Lin, D., Cai, J., Guo, Z., Zeng, F., An, F., Liu, H., 2013. Evaluation of landslide risk based on synchronization of nonlinear motions in observed data. Nat. Hazards 65 (1), 581–603.
Liu, T., Deng, J., Zheng, J., Zheng, L., Zhang, Z., Zheng, H., 2017. A new semi-deterministic block theory method with digital photogrammetry for stability analysis of a high rock slope in China. Eng. Geol. 216, 76–89.
Liu, L., Yin, H., Xiao, T., Huang, L., Cheng, Y., 2024. Dynamic prediction of landslide life expectancy using ensemble system incorporating classical prediction models and machine learning. Geosci. Front. 15 (2), 101758.
Ma, J., Tang, H., Liu, X., Wen, T., Zhang, J., Tan, Q., Fan, Z., 2018. Probabilistic forecasting of landslide displacement accounting for epistemic uncertainty: a case study in the three Gorges reservoir area, China. Landslides 15 (6), 1145–1153.
Manconi, A., Giordan, D., 2016. Landslide failure forecast in near-real-time. Geomat. Nat. Hazards Risk 7 (2), 639–648.
Massironi, M., Zampieri, D., Superchi, L., et al., 2013. Geological structures of the vajont landslide. Ital. J. Eng. Geol. Environ. 6, 573–582.
Metropolis, N., Rosenbluth, A., Rosenbluth, M., Teller, A., Teller, E., 1953. Equation of state calculations by fast computing machines. J. Chem. Phys. 21 (6), 1087–1092.
Mufundirwa, A., Fujii, Y., Kodama, J., 2010. A new practical method for prediction of geomechanical failure-time. Int. J. Rock Mech. Min. Sci. 47 (7), 1079–1090.
O'Dowd, N., Madarshahian, R., Leung, M., Corcoran, J., Todd, M., 2021. A probabilistic estimation approach for the failure forecast method using Bayesian inference. Int. J. Fatigue 142, 105943.
Paronuzzi, P., Bolla, A., Rigo, E., 2016. Brittle and ductile behavior in deep-seated landslides: learning from the vajont experience. Rock Mech. Rock Eng. 49 (6), 2389–2411.
Pecoraro, G., Calvello, M., Piciullo, L., 2019. Monitoring strategies for local landslide early warning systems. Landslides 16 (2), 213–231.
Pilgrim, C., 2021. Piecewise-regression (aka segmented regression) in python. J. Open Source Softw. 6 (68), 3859.
Qin, S., Jiao, J., Li, Z., 2006. Nonlinear evolutionary mechanisms of instability of plane-shear slope: Catastrophe, bifurcation, chaos and physical prediction. Rock Mech. Rock Eng. 39 (1), 59–76.
Rose, N., Hungr, O., 2007. Forecasting potential rock slope failure in open pit mines using the inverse-velocity method. Int. J. Rock Mech. Min. Sci. 44 (2), 308–320.
Saito, M., 1965. Forecasting the time of occurrence of a slope failure. In: Proceedings of the 6th International Conference on Soil Mechanics and Foundation Engineering, pp. 537–541. Montreal, Canada.
Sammis, C., Sornette, D., 2002. Positive feedback, memory, and the predictability of earthquakes. Proc. Natl. Acad. Sci. USA 99 (Suppl. 1), 2501–2508.
Sättele, M., Krautblatter, M., Bründl, M., Straub, D., 2016. Forecasting rock slope failure: how reliable and effective are warning systems? Landslides 13 (4), 737–750.
Scoppettuolo, M., Cascini, L., Babilio, E., 2020. Typical displacement behaviours of slope movements. Landslides 17 (5), 1105–1116.
Segalini, A., Valletta, A., Carri, A., 2018. Landslide time-of-failure forecast and alert threshold assessment: a generalized criterion. Eng. Geol. 245, 72–80.
Sharifi, S., Macciotta, R., Hendry, M., 2022. Algorithms to enhance detection of landslide acceleration moment and time-to-failure forecast using time-series displacements. Eng. Geol. 309, 106832.
Sharifi, S., Macciotta, R., Hendry, M., 2024. Critical assessment of landslide failure forecasting methods with case histories: a comparative study of INV, MINV, SLO, and VOA. Landslides 21 (7), 1629–1643.
Shen, Y., Wu, S., Cheng, H., Zhang, H., Wang, J., Yang, Z., Song, X., 2023. Uncertainty analysis method of slope safety factor based on quantile-based ensemble learning. Bull. Eng. Geol. Environ. 82 (3), 87.
Silva, A., Sotomayor, J., Torres, V., 2021. Correlations of geotechnical monitoring data in open pit slope back-analysis: a mine case study. J. South. Afr. Inst. Min. Metall. 121 (10), 557–564.
Sullivan, T., 2007. Hydromechanical coupling and pit slope movements. In: Proceedings of the 2007 International Symposium on Rock Slope Stability in Open Pit Mining and Civil Engineering, pp. 3–43. Perth, Australia.
Voight, B., 1988. A method for prediction of volcanic eruptions. Nature 332 (6160), 125–130.
Wang, H., Zhong, P., Xiu, D., Xiu, D., Zhong, Y., Peng, D., Xu, Q., 2022. Monitoring tilting angle of the slope surface to predict loess fall landslide: an on-site evidence from Heifangtai loess fall landslide in Gansu province, China. Landslides 19, 719–729.
Wang, J., Dong, L., Ji, S., 2025. Rock mass instability early warning model: a case study of a high and steep annular slope mining areas using Sen's slope trend analysis. Tunn. Undergr. Space Technol. 159, 106514.
Wang, L., Xiao, T., Liu, S., Zhang, W., Yang, B., Chen, L., 2023. Quantification of model uncertainty and variability for landslide displacement prediction based on Monte Carlo simulation. Gondwana Res. 123, 27–40.
Welch, G., Bishop, G., 1995. An Introduction to the Kalman Filter. University of North Carolina, Chapel Hill, USA.
Xie, J., Uchimura, T., Wang, G., et al., 2020. A new prediction method for the occurrence of landslides based on the time history of tilting of the slope surface. Landslides 17, 301–312.
Xu, Q., Zhao, B., Dai, K., et al., 2023. Remote sensing for landslide investigations: a progress report from China. Eng. Geol. 321, 107156.
Xu, Q., Yuan, Y., Zeng, Y., Hack, R., 2011. Some new pre-warning criteria for creep

slope failure. Sci. China Technol. Sci. 54, 210–220.
Yan, B., 2021. MT-InSAR Technology Combined with inverse-velocity Method for high-level Landslide Monitoring and Early Warning. Southwest Jiaotong University. MSc Thesis. Chengdu, China (in Chinese).
Yu, X., Zhao, Q., Zhang, C., Liu, J., 2019. Application of GNSS real-time monitoring in landslide early warning: case of landslide of G108 section in Zhouzhi county, Shannxi province. Yangtze River 50 (10), 126–130 (in Chinese).
Zhang, H., Wu, S., Zhang, X., Han, L., Zhang, Z., 2022a. Slope stability prediction method based on the margin distance minimization selective ensemble. Catena 212, 106055.
Zhang, H., Wu, S., Zhang, Z., Huang, S., 2023. Reliability analysis of rock slopes considering the uncertainty of joint spatial distributions. Comput. Geotech. 161, 105566.
Zhang, J., Tang, H., Li, C., Gong, W., Zhou, B., Zhang, Y., 2024b. Deformation stage division and early warning of landslides based on the statistical characteristics of landslide kinematic features. Landslides 21 (4), 717–735.
Zhang, J., Wang, Z., Hu, J., Xiao, S., Shang, W., 2022b. Bayesian machine learning-based method for prediction of slope failure time. J. Rock Mech. Geotech. Eng. 14 (4), 1188–1199.
Zhang, J., Wang, Z., Zhang, G., Xue, Y., 2020. Probabilistic prediction of slope failure time. Eng. Geol. 271, 105586.
Zhang, W., Liu, S., Wang, L., Sun, W., He, Y., Wang, Y., Sun, G., 2024a. The overall stability of a partially unstable reservoir bank slope to water fluctuation and rainfall based on Bayesian theory. Landslides 21 (8), 2021–2032.
Zheng, J., Kulatilake, P., Shu, B., Sherizadeh, T., Deng, J., 2014. Probabilistic block theory analysis for a rock slope at an open pit mine in USA. Comput. Geotech. 61, 254–265.
Zheng, J., Kulatilake, P., Deng, J., 2015. Development of a probabilistic block theory analysis procedure and its application to a rock slope at a hydropower station in China. Eng. Geol. 188, 110–125.
Zheng, Z., Deng, B., Liu, H., Wang, W., Huang, S., Li, S., 2024a. Microdynamic mechanical properties and fracture evolution mechanism of monzogabbro with a true triaxial multilevel disturbance method. Int. J. Min. Sci. Technol. 34 (3), 385–411.
Zheng, Z., Li, R., Pan, P., Qi, J., Su, G., Zheng, H., 2024b. Shear failure behaviors and degradation mechanical model of rockmass under true triaxial multi-level loading and unloading shear tests. Int. J. Min. Sci. Technol. 34 (10), 1385–1408.
Zhou, C., Cao, Y., Gan, L., Wang, Y., Motagh, M., Roessner, S., Hu, X., Yin, K., 2024a. A novel framework for landslide displacement prediction using MT-InSAR and machine learning techniques. Eng. Geol. 334, 107497.
Zhou, C., Chen, Y., Jiang, Q., Lu, W., 2011. A generalized multi-field coupling approach and its application to stability and deformation control of a high slope. J. Rock Mech. Geotech. Eng. 3 (3), 193–206.
Zhou, X., Yuan, X., Yang, D., 2024b. Prediction of landslide failure time based on moving average convergence and divergence coupling with Bayesian updating method. Eng. Geol. 343, 107781.
Zhu, H., Ye, X., Pei, H., Zhang, W., Cheng, G., Li, Z., 2024. Probing multi-physical process and deformation mechanism of a large-scale landslide using integrated dual-source monitoring. Geosci. Front. 15 (2), 101773.

Mingxi Chen received his PhD degree in Geotechnical Engineering from the School of Civil Engineering at Wuhan University (China) in 2022. He obtained his BSc degree in Engineering from the School of Geosciences and Info-physics at Central South University (China) in 2016. He is now an assistant professor of the School of Civil Engineering and Architecture at Guangxi University (China). His main research interests include: (1) deformation mechanism and stability evaluation of high steep slopes in hydropower projects; (2) prediction and early warning of landslides; and (3) nonlinear dynamic evolution mechanism of deformation and failure in rock mass.